Global spectral classification of Martian low-albedo regions with Mars Global Surveyor Thermal Emission Spectrometer (MGS-TES) data

A. Deanne Rogers,[1] Joshua L. Bandfield,[2] and Philip R. Christensen[2]

Received 4 April 2006; revised 12 August 2006; accepted 13 September 2006; published 14 February 2007.

[1] Martian low-albedo surfaces (defined here as surfaces with Mars Global Surveyor Thermal Emission Spectrometer (MGS-TES) albedo values $\leq$0.15) were reexamined for regional variations in spectral response. Low-albedo regions exhibit spatially coherent variations in spectral character, which in this work are grouped into 11 representative spectral shapes. The use of these spectral shapes in modeling global surface emissivity results in refined distributions of previously determined global spectral unit types (Surface Types 1 and 2). Pure Type 2 surfaces are less extensive than previously thought, and are mostly confined to the northern lowlands. Regional-scale spectral variations are present within areas previously mapped as Surface Type 1 or as a mixture of the two surface types, suggesting variations in mineral abundance among basaltic units. For example, Syrtis Major, which was the Surface Type 1 type locality, is spectrally distinct from terrains that were also previously mapped as Type 1. A spectral difference also exists between southern and northern Acidalia Planitia, which may be due in part to a small amount of dust cover in southern Acidalia. Groups of these spectral shapes can be averaged to produce spectra that are similar to Surface Types 1 and 2, indicating that the originally derived surface types are representative of the average of all low-albedo regions.

Citation: Rogers, A. D., J. L. Bandfield, and P. R. Christensen (2007), Global spectral classification of Martian low-albedo regions with Mars Global Surveyor Thermal Emission Spectrometer (MGS-TES) data, *J. Geophys. Res.*, *112*, E02004, doi:10.1029/2006JE002726.

1. Introduction

1.1. Overview

[2] One of the major science objectives of the Mars Global Surveyor Thermal Emission Spectrometer (MGS-TES) investigation is to map the mineralogy of surface soils and rocks [*Christensen et al.*, 1992, 2001], in order to improve understanding of Martian crust and mantle composition and evolution, and surface weathering. To address this objective, methods were developed for removing atmospheric components from TES spectra [*Bandfield et al.*, 2000a; *Smith et al.*, 2000a; *Ruff and Christensen*, 2002; *Bandfield and Smith*, 2003] and measuring global variations in surface mineralogy and spectral response [*Bandfield et al.*, 2000b; *Bandfield*, 2002; *Rogers and Christensen*, 2003]. Plagioclase feldspar was found to be a major component of almost all Martian dark regions [*Christensen et al.*, 2000a; *Bandfield*, 2002], and potentially a component of the globally homogeneous surface dust [*Ruff and Christensen*, 2002; *Bandfield et al.*, 2003; *Bandfield and Smith*, 2003]. As has been determined with VIS/NIR observations [e.g., *Adams*, 1968; *McCord et al.*, 1978; *Singer*, 1982; *Soderblom*,1992; *Erard et al.*, 1990; *Bell et al.*, 1997; *Mustard et al.*, 1997; *Bibring et al.*, 2005; *Mustard et al.*, 2005], pyroxenes were also found to be a significant mineral phase for most Martian low-albedo regions, whereas olivine and sheet silicates were not found in abundance [*Soderblom*, 1992; *Bandfield et al.*, 2000b; *Christensen et al.*, 2000a; *Bandfield*, 2002].

[3] From TES-derived global mineral maps [*Bandfield*, 2002, 2003], it is apparent that there are variations in the mineral assemblages from dark regions. Plagioclase is found in significant concentrations in all low-albedo regions, whereas high-Ca clinopyroxenes are largely confined to low-albedo regions in the southern highlands [*Bandfield*, 2002; *Rogers and Christensen*, 2003]. Primary high-silica volcanic glasses are similar in spectral character to some sheet silicates [*Bandfield*, 2002; *Wyatt and McSween*, 2002] secondary amorphous silica [e.g., *Wyatt and McSween*, 2002; *Kraft et al.*, 2003], zeolites [*Ruff*, 2004], and poorly crystalline aluminosilicates in weathering rinds [*Kraft et al.*, 2005; *Michalski et al.*, 2005a]. These ''high-silica phases,'' with an implied Si/O > $\sim$0.35 [*Michalski et al.*, 2005b], are found scattered throughout all low-albedo regions at $\sim$15–20%, with the highest concentrations in Acidalia Planitia and the north polar sand dunes [*Bandfield*, 2002; *Bandfield et al.*, 2002].

[4] Finally, *Bandfield et al.* [2000b] determined that the spectral response from Martian low-albedo regions could generally be grouped into two classes: Surface Type 1, which is largely confined to the southern highlands, with a

[1]Division of Geological and Planetary Sciences, California Institute of Technology, Pasadena, California, USA.
[2]Department of Geological Sciences, Arizona State University, Tempe, Arizona, USA.

0148-0227/07/2006JE002726$09.00

few isolated exceptions in the northern lowlands [*Rogers and Christensen*, 2003], and Surface Type 2, which is primarily concentrated in the northern lowlands, but also has significant concentrations scattered throughout the southern highlands. Surface Type 1 has been interpreted as basalt to basaltic andesite [*Bandfield et al.*, 2000b; *Christensen et al.*, 2000a; *Hamilton et al.*, 2001; *Wyatt and McSween*, 2002], whereas Surface Type 2 has been interpreted as basaltic andesite to andesite [*Bandfield et al.*, 2000b; *Hamilton et al.*, 2001, 2003a; *McSween et al.*, 2003] or altered basalt [*Wyatt and McSween*, 2002; *McSween et al.*, 2003; *Morris et al.*, 2003; *Kraft et al.*, 2003; *Michalski et al.*, 2005b].

1.2. Objective and Motivation for This Study

[5] At a spatial resolution of 1 pixel-per-degree (ppd), *Bandfield et al.* [2000b] found that all low-albedo regions may be modeled with RMS errors < ~0.5% using only Surface Types 1 and 2 and hematite, indicating that there are no regions of extreme spectral differences from these end-members, such as those that would be caused by a large exposure of silicic crustal rocks or sediments, clays or carbonate. However, if small but geologically significant differences in the characteristic mineralogy of Surface Types 1 and 2 are present, for example a 10% increase in pyroxene abundance, RMS errors below 0.5% can be maintained.

[6] Several detailed analyses of some low-albedo regions have identified local occurrences of mineralogies unique from Surface Types 1 and 2, such as olivine basalts [*Christensen et al.*, 2003; *Hamilton et al.*, 2003b; *Hoefen et al.*, 2003; *Bibring et al.*, 2005; *Christensen et al.*, 2005; *Hamilton and Christensen*, 2005; *Mustard et al.*, 2005; *Rogers et al.*, 2005] and quartz-rich terrains [*Bandfield et al.*, 2004]. In addition, larger regions have been shown to have subtle spectral differences from the global end-members, including Solis Planum [*Bandfield*, 2002], Ares Vallis [*Rogers et al.*, 2005], and Aram Chaos [*Glotch and Christensen*, 2005]. Locations within Ares Vallis and Aram Chaos are modeled better with a set of mineral spectra than with only the global end-members, suggesting that they may differ in primary mineralogy or alteration history from areas that exhibit the typical spectral character of Surface Types 1 and 2.

[7] In addition to the motivation listed above, there are other reasons to reexamine the surface emissivity from Martian low-albedo regions. Since the initial work of *Bandfield et al.* [2000b], the ASU mineral library [*Christensen et al.*, 2000b] has been updated to include spectral data from 220–2000 cm^{-1}, providing nine more spectral channels (from ~300–400 cm^{-1}) at 10 cm^{-1} sampling available for TES data analysis. Second, additional orbits are available for use, between ~3100 and 5317. Beginning around orbit 5317, spacecraft-induced spectral artifacts become more common in the TES data [*Bandfield*, 2002; *Hamilton et al.*, 2003b]. The primary benefit of having these extra ~2200 orbits is additional spatial coverage in the southern hemisphere during the southern summer. Finally, additional library spectra are now available, including spectra from an olivine solid-solution series [*Hamilton and Schneider*, 2005], Si-K glass and SiO_2 glass [*Wyatt et al.*, 2001], opaline materials [*Michalski et al.*, 2003], smectites [*Michalski et al.*, 2005b], shocked feldspars [*Johnson et al.*, 2002a] and a globally uniform surface dust end-member [*Bandfield and Smith*, 2003]. Note that the increased spectral range, additional orbits, and some of these new spectra were included in the mineral mapping study of *Bandfield* [2002].

[8] This study builds on the previous work of *Bandfield et al.* [2000b] by refining the distributions of pure Type 1 and 2 surfaces and reporting regional spectral deviations from these two types. Where possible, multiple surface-atmosphere separation techniques are used to validate the surface emissivity variations derived in this work, therefore a review of previously developed methods is provided (section 2.2). Finally, the primary surface-atmosphere separation method used in this work is linear deconvolution [e.g., *Smith et al.*, 2000a]. In section 3, atmospheric and surface characteristics that affect the derivation of surface emissivity using that method are examined in detail.

[9] In summary, the major components of this work are: (1) a reexamination of low-albedo regions to define regional surface types; (2) detailed global mapping of the subtle variations in spectral character; and (3) a review of TES surface-atmosphere separation techniques and in particular, the linear deconvolution technique. Derivation and discussion of surface mineralogy and geologic context are provided in a companion paper [*Rogers and Christensen*, 2007] (hereinafter referred to as Paper 2).

2. Background

2.1. TES Instrument Description

[10] The TES instrument consists of a Fourier-transform Michelson infrared interferometric spectrometer, and co-aligned visible/near-infrared and thermal infrared radiometers. The spectrometer is used to obtain IR radiance spectra at a selectable spectral sampling of 5 or 10 cm^{-1} between 1650 and 200 cm^{-1} (5.8 to 50 μm) [*Christensen et al.*, 2001]. The broadband radiometers are used to measure bolometric visible/near-infrared reflectance (0.3–2.9 μm, albedo) and thermal radiance (5.1 to >100 μm) of the surface. The six detectors for each of the three instrument components are arranged in a 3 × 2 array, and each have a spatial footprint of 3 × ~8 km (cross-track by along-track dimensions) from the MGS mapping phase altitude of 378 km [*Christensen et al.*, 2001]. TES hyperspectral radiance spectra are converted to effective emissivity spectra (also referred to as "equivalent emissivity" [e.g., *Bandfield et al.*, 2004] or "apparent emissivity" [e.g., *Ruff and Christensen*, 2002]) using the method described by *Christensen* [1998].

2.2. Review of TES Surface-Atmosphere Separation Techniques

2.2.1. Multiple Emission Angle Surface-Atmosphere Separation

[11] TES spectra of Mars contain atmospheric and surface contributions to the observed radiance. One of the TES observing strategies to separate these contributions is to acquire spectra from the same surface at varying emission angles (referred to as EPF, for emission phase function) [*Christensen et al.*, 2001; *Bandfield and Smith*, 2003]. This requires movement of the TES pointing mirror to the forward, nadir, and aft direction as the Mars Global Sur-

veyor spacecraft crosses over the surface of interest. Using this technique, surface emissivity may be well-constrained through a set of 3–20 same-surface observations where only the atmospheric path length is varying. The advantages are that (1) no assumptions about the surface emissivity or the spectral shape of atmospheric components are required, (2) subtle surface emissivity features from high-albedo regions may be derived, and (3) surface emissivity may be derived over an increased spectral range [*Bandfield and Smith*, 2003]. The major disadvantage is that special observation strategies are required and so this technique cannot be applied globally. In addition, the presence of water ice in the EPF measurement may adversely affect the derived surface emissivity. Finally, the EPF method assumes that the surface of interest is uniform in composition; any variability could introduce error in the surface-atmosphere separation calculation [*Bandfield and Smith*, 2003]. On Mars, many low-albedo regions are likely to be heterogeneous in composition and/or temperature at the scale of the EPF observation footprint, whereas bright regions are usually homogeneous. As a result, this technique is best used for determination of high-albedo region surface emissivity [*Bandfield and Smith*, 2003]. The surface emissivity of Martian high-albedo surfaces has been well constrained using the EPF method, and was shown to be relatively constant within high-albedo regions [*Bandfield and Smith*, 2003]. Confirmation of this spectral shape was determined from the Martian surface at both the MER Spirit and Opportunity landing sites with the Mini-TES instrument [*Christensen et al.*, 2004a, 2004b]. In this work we refer to the average high-albedo surface emissivity spectrum of *Bandfield and Smith* [2003] as "EPF surface dust."

2.2.2. Linear Deconvolution

[12] The linear deconvolution method described by *Bandfield et al.* [2000b] and *Smith et al.* [2000a] uses a spectral library of potential surface end-members, atmospheric end-members [*Bandfield et al.*, 2000a; *Bandfield*, 2002], and a blackbody spectrum to obtain a linear least squares fit to the measured TES effective emissivity spectrum. The atmospheric component spectra are scaled according to their modeled concentrations and removed from the measured spectrum to produce a surface-only emissivity spectrum. Negative concentrations of atmospheric components are allowed to account for measured spectra with atmospheric conditions (example: lower opacities) beyond those spanned by the atmospheric end-members [*Bandfield*, 2002]. The linear deconvolution atmosphere removal technique can be applied on a spectrum-by-spectrum basis or on binned spectral emissivity data, because atmospheric components combine in an approximately linear fashion (excluding spectra taken of surfaces $<\sim$240K or during periods of high atmospheric dust or water ice loadings) [*Bandfield et al.*, 2000b; *Bandfield*, 2002]. Finally, no special observing strategies are required. The disadvantages are that (1) the actual surface components must be present in the spectral library and (2) the derived surface shape could contain small residual atmospheric absorptions or false surface emissivity features due to minor overcorrection or undercorrection for a particular atmospheric component. Potential causes for these overcorrections or undercorrections and suggestions for minimizing these errors are given in section 3.

[13] The linear deconvolution algorithm returns the modeled spectrum, atmosphere-removed surface emissivity and modeled surface spectrum, a set of end-member and blackbody concentrations, and RMS (root-mean-square) error. Interpretation of spatial variation in end-member concentrations and RMS error requires consideration of spatial variations in surface spectral contrast, described below.

[14] The best way to evaluate the model fit is to compare the modeled emissivity spectrum to the measured spectrum [e.g., *Gillespie*, 1992; *Ramsey and Christensen*, 1998]. Visual inspection of the spectra for features that are not well-modeled gives some indication of missing components from the spectral library [*Ramsey and Christensen*, 1998]. This modeled-measured difference for a spectrum with (m) number of channels may also be represented as a single value using an RMS error calculation [*Ramsey and Christensen*, 1998],

$$\mathrm{RMS} = \sqrt{\sum_{j=1}^{m} \left(\varepsilon_{\mathrm{j,\,meas.}} - \varepsilon_{\mathrm{j,\,model.}}\right)^2 / \mathrm{m}}. \quad (1)$$

[15] RMS error is a useful parameter for spatial comparison of quality-of-fit [*Bandfield et al.*, 2000b; *Bandfield*, 2002; *Hamilton et al.*, 2003b]. However, spatial comparisons of RMS error can be misleading if relative differences in spectral contrast are not considered [e.g., *Koeppen and Hamilton*, 2005]. Linear least squares fitting of two spectra that have identical shapes but a difference in magnitude of spectral feature depth would yield identical normalized modal mineralogy results and modeled emissivity, however the calculated RMS error value would be higher for the spectrum with deeper features.

[16] The original surface and atmosphere concentrations output from the model are not normalized for blackbody and are representative of the percentage of each end-member that contributes to the modeled spectrum [e.g., *Hamilton et al.*, 2003b]. Concentration values are best for determining the significance of the contribution of each end-member to the measured spectrum; however, one disadvantage to interpreting concentrations is that two surfaces of slightly different spectral contrast but identical mineralogy would show apparent differences in mineral quantity. For true spatial comparisons of modal mineralogy between these surfaces, the concentrations can be converted to "abundance" [*Hamilton et al.*, 2003b] by normalizing surface spectral concentrations for blackbody and atmospheric concentrations. In converting concentration values to abundance, values that may have been below the estimated detection limit (0.10 [*Bandfield*, 2002]) will be inflated. Thus, for cases where the surface component has a relatively low contribution to the measured spectrum (i.e., surfaces with low spectral contrast), abundances should be interpreted with caution.

2.2.3. Spectral Ratios

[17] Spectra from surfaces of differing spectral contrast that are near each other both in elevation and lateral distance may be ratioed to cancel atmospheric components and produce a ratio–surface spectrum [e.g., *McCord*, 1969; *McCord and Westphal*, 1971; *Pollack et al.*, 1990; *Moersch et al.*, 1997; *Hoefen et al.*, 2003; *Johnson et al.*, 2002b; *Ruff and Christensen*, 2002; *Mustard et al.*, 2005]. If properly

applied, the advantage of this technique is the lack of residual atmospheric features in the derived ratio spectrum. However, the disadvantage is that very specific conditions are required: the two spectra used in the ratio must (1) be from the same orbit, (2) be from surfaces that are proximal to each other in spatial distance and elevation, (3) have no small-scale variation in atmospheric dust or water ice, and (4) be from surfaces that are similar in temperature [*Johnson et al.*, 2002b; *Ruff and Christensen*, 2002]. Finally, ratio spectra can be difficult to interpret, because features from both surfaces will be present in the ratio. However, if one of the surfaces is spectrally grey and near-unity emissivity, as is nearly the case for dust-covered (high-albedo) surfaces between $\sim$200–1300 cm^{-1}, the ratio spectrum should be dominated by features of the lower albedo surface. Although there are features present in spectra from dust-covered surfaces within this wavelength region [*Ruff and Christensen*, 2002; *Bandfield and Smith*, 2003], they are small in magnitude relative to spectral features from coarse-particulate surfaces and therefore a ratio spectrum of high- and low-albedo surfaces may be used to determine, to first order, a surface emissivity shape.

2.2.4. Radiative Transfer

[18] The radiative transfer method [*Smith et al.*, 2000a] is essentially a "boot-strap" technique where dust, water ice, and surface spectral shapes are successively derived. TES radiance spectra are first converted to opacity spectra [*Smith et al.*, 2000b]. The average dust opacity spectrum is derived from a small, high-albedo region that is known to have infrequent water ice cloud occurrence. Next, to find the water ice spectral shape, spectra are selected from a high-albedo, typically cloudy region. The dust and water ice mixing coefficient is determined and the water ice spectral shape is derived. Finally, the surface opacity spectral shape from the low-albedo region of interest is derived in a similar manner to that used for water ice, and converted to surface emissivity. A detailed description of the radiative transfer method is given by *Smith et al.* [2000a].

2.2.5. Factor Analysis and Target Transformation

[19] The factor analysis and target transformation method [*Bandfield et al.*, 2000a; *Smith et al.*, 2000a] uses a set of several hundred to thousands of mixed spectra that contain independently varying components. Applied to the TES spectra, the varying components are atmospheric dust, water ice, surface emissivity, and in some cases, surface phases or assemblages that vary independently of the average background surface emissivity, such as hematite [*Bandfield et al.*, 2000a; *Christensen et al.*, 2000c; *Glotch et al.*, 2004]. Factor analysis is used to determine the number of independently varying components present in the set of mixed spectra. The target transformation step takes the minimum number of eigenvectors required to reconstruct the original set of mixed spectra to within the noise, and applies a linear least squares fit to a trial spectrum. The trial spectrum is a best guess of one of the independently varying components. If the trial spectrum is fit well by the eigenvectors, then that trial spectrum is potentially one of the spectral end-members present in the data. If the trial spectrum is not well fit by the eigenvectors, the best fit spectrum is commonly a close approximation of the actual end-member. The correct end-member may be recovered by inspection of all of the best fit spectra for the trial spectrum and isolating linearly independent end-members from recurrent best fit spectra. The disadvantage of this technique is that usually several hundred spectra are needed; however, this technique could be useful for deriving a surface spectral shape from slightly higher-albedo regions or to confirm linear deconvolution-derived surface emissivity. In addition, it may be used to identify an independently varying component within a given region.

2.3. Mineral and Surface Spectral Mapping Techniques

2.3.1. Spectral Classification of Martian Low-Albedo Regions

[20] *Bandfield et al.* [2000b] examined spectra from individual orbits over 25 low-albedo regions. For each orbit, surface emissivity spectra were retrieved using the linear deconvolution method. Data used to derive these spectra were constrained on dust opacity <0.3, ice opacity <0.1, TES albedo <0.15 and surface temperatures > 270 K. Upon examination of the average surface spectra from each dark region, *Bandfield et al.* [2000b] determined that the spectra could be divided into two end-member classes, Surface Types 1 and 2. Global average end-members that represent each of those classes were produced by averaging four to seven of the 25 average dark region spectra. Other dark region spectra were averaged and classified as intermediate between the two end-members. *Bandfield et al.* [2000b] derived modal mineralogies for each of the two surface types using the linear deconvolution method [e.g., *Ramsey and Christensen*, 1998]. The global distributions of these average surface shapes were determined by adding these to an end-member set with target transformation-derived Meridiani hematite [*Christensen et al.*, 2000c], and four previously isolated atmospheric spectral shapes [*Bandfield et al.*, 2000a], and deconvolving $\sim 10^7$ individual TES spectra. The output was a database of surface type concentrations and RMS error, which were then binned and mapped at a spatial resolution of one pixel-per-degree.

2.3.2. Mineral Mapping

[21] A second method of displaying global surface composition is to derive mineral maps. *Bandfield* [2002, 2003] derived mineral concentration maps using a data reduction strategy of first binning effective emissivity spectra and then applying the linear deconvolution algorithm to each average spectrum. *Bandfield* [2002, 2003] used a library of potential surface spectral components (minerals [*Christensen et al.*, 2000b], glasses and EPF surface dust [*Bandfield*, 2003; *Bandfield and Smith*, 2003]), previously isolated atmospheric dust and water ice end-members [*Bandfield et al.*, 2000a], synthetic atmospheric water vapor and CO_2 [*Bandfield*, 2002], and blackbody. Note that mineral concentration maps were intentionally not renormalized to 100% after removal of blackbody and atmospheric concentrations, because unnormalized concentrations more appropriately reflect the true contribution of each mineral spectrum to the modeled TES spectrum. Therefore interpretation of these maps in terms of relative mineral abundance is not straightforward, and spectral contrast of the surface (or amount of blackbody contribution to the spectrum) should be taken into consideration when comparing mineral concentrations above the detection limit from region to region (section 2.2.2).

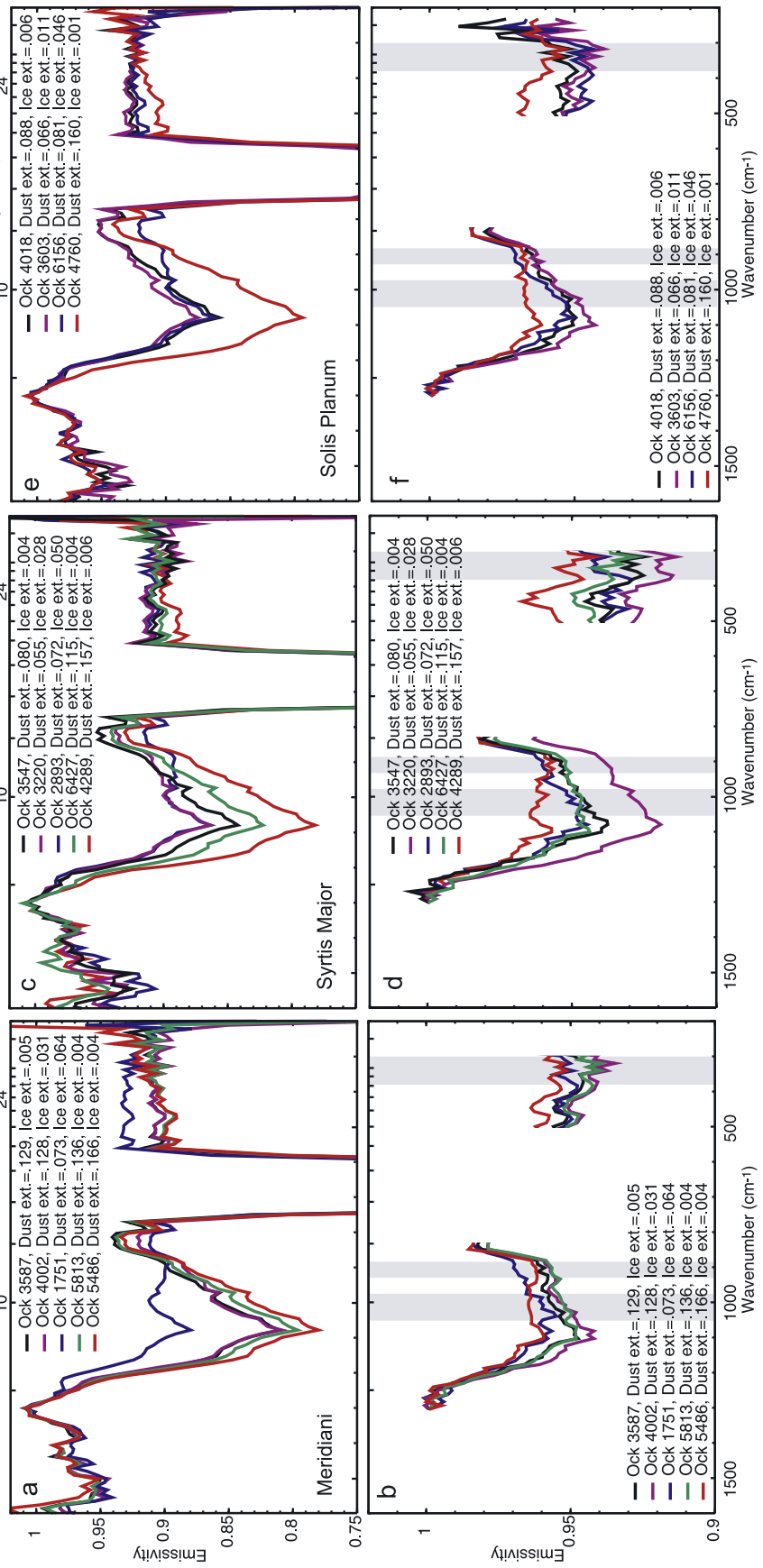

Figure 1. Illustration of atmospheric influence on derived surface emissivity. TES spectra from a region in Sinus Meridiani (−3.34°S to −2.24°S, 7.23°E to 7.73°E, IAU 2000 coordinates), Syrtis Major (14.40°N to 14.68°N, 69.56°E to 70.09°E, IAU 2000), and Solis Planum (−27.6°S to −27.5°S, 272.8°E to 273.0°E, IAU 2000). (a, c, e). Average effective emissivity spectra from four to five different orbits. Each spectrum is the average of (Figure 1a) 9–12 consecutive ICKs (~54–72 spectra) (Meridiani example) or (Figure 1b) the average of six spectra (Syrtis and Solis examples), and contains a different amount of dust and/or water ice contribution. (b, d, f) Derived surface emissivity using the linear deconvolution method for each orbit. No contrast enhancement or offset was applied. The shaded areas are wavelength regions of derived surface emissivity where, in these examples, effects from increased water ice and atmospheric dust contribution are most apparent (see text).

Table 1. Spectral Library[a]

Mineral Group	Potential End-Member
Quartz	Quartz BUR-4120
Feldspar	Microcline BUR-3460
	Orthoclase WAR-RGSAN01(a)
	Albite WAR-0244
	Oligoclase WAR-5804
	Andesine BUR-240
	Labradorite WAR-4524
	Bytownite WAR-1384
	Anorthite BUR-340
	Shocked An 22.6 Gpa(b)
	Shocked An 56.3 GPa(b)
Orthopyroxene	Bronzite NMNH-93527
	Enstatite HS-9.4B
	Bronzite BUR-1920
Clinopyroxene	Diopside WAR-6474
	Augite NMNH-9780(c)
	Augite NMHN-122302(c)
	Hedenbergite manganoan DSM-HED01
	Pigeonite(c)
Olivine	Forsterite BUR-3720A
	Fayalite WAR-RGFAY01
	KI 3362 Fo60(d)
	KI 3115 Fo68(d)
	KI 3373 Fo35(d)
	KI 3008 Fo10(d)
Zeolite	Crystalline heulandite(e)
	Crystalline stilbite(e)
Sheet silicates	Biotite BUR-840
	Muscovite WAR-5474
	Serpentine HS-8.4B
	Antigorite NMNH-47108
	Illite granular IMt-2 minus 60%bb[b]
	Ca-montmorillonite solid STx-1
	saponite <0.2 mic plus 60%bb(f)[b]
Amorphous silica	K-rich Glass(g)
	SiO2 Glass(g)
	opal-A (01-011)(h)
	Al-Opal(i)
Amphibole	Magnesiohastingsite HS-115.4B
	Actinolite HS-116.4B
	Magnesiohornblende WAR-0354
Hematite	Average Martian Hematite(j)
Carbonate	Calcite C40
	Dolomite C20
Sulfate	Anhydrite ML-S9
	Gypsum ML-S6
Surface dust	Average high albedo surface(k)
Atmosphere	low-opacity dust
	high-opacity dust
	water ice (small)
	water ice (large)
	synthetic CO_2
	synthetic water vapor
Blackbody	blackbody

[a]Mineral spectra are from the ASU spectral library available online at http://tes.asu.edu [*Christensen et al.*, 2000b], with the following exceptions: (a) provided by S. W. Ruff, samples described by *Ruff* [1998]; (b) *Johnson et al.* [2002a]; (c) provided by V. E. Hamilton, described by *Hamilton* [2000]; (d) provided by V. E. Hamilton, samples described by *Morse* [1996]; (e) described by *Ruff* [2004]; (f) described by *Michalski et al.* [2005b]; (g) described by *Wyatt et al.* [2001]; (h) described by *Michalski et al.* [2003]; (i) provided by M. D. Kraft (personal communication, 2005); (j) derived from TES data, described by *Glotch et al.* [2004]; (k) derived from emission phase function observations with TES by *Bandfield and Smith* [2003].

[b]Blackbody was subtracted from the spectrum to produce comparable spectral contrast to that of other solid clays in the ASU library.

2.4. Summary

[22] In summary, several techniques are available for separating atmospheric and surface components in TES data. Some techniques are better suited for determining surface emissivity of bright regions, whereas others are better suited for dark regions. The type of technique chosen for use requires consideration of the nature of the surface of interest, and also the scale of the study (e.g., global, local). Where possible, multiple techniques should be used to build confidence in the derived surface emissivity spectrum. The focus of this work is to determine the surface emissivity and mineralogy of low-albedo regions, at a global scale. Therefore we primarily use the linear deconvolution surface-atmosphere separation strategy. Spectral ratios are also used to corroborate surface emissivity shapes derived using the deconvolution method, where possible. Potential influences on derived surface emissivity from various atmospheric and surface conditions when using the linear deconvolution method are examined in section 3.0.

[23] Two global mapping strategies were discussed above. In one, low-albedo regions were classified into two groups by their characteristic surface emissivity, and mineralogy was determined from the two average spectral shapes. Concentrations of each of these end-members were derived from deconvolving millions of individual TES spectra, and the distributions of these concentrations were globally mapped. In the second method, millions of TES spectra were first binned at a resolution of one pixel-per-degree, then a library of mineral and atmospheric spectra were used to model the binned TES spectra. In this work we use aspects of both techniques (section 4).

3. Influences on Surface Emissivity Derivation

[24] Linear deconvolution is the primary technique used in this work. Here we examine the accuracy of surface-atmosphere separation where using the linear deconvolution method (1) under various levels of contribution from atmospheric dust and water ice, (2) with negative atmospheric end-member concentrations allowed and not allowed, and (3) over surfaces with low spectral contrast. Examples from every combination of conditions and a quantitative assessment of uncertainty are not practical and therefore not provided here. Instead, only a demonstration of the general trends and degree of influence on derived surface emissivity from these effects are presented.

3.1. Excessive Atmospheric Dust and Water Ice

[25] Data selection criteria for previous composition maps derived using TES data were purposefully inclusive, in terms of atmospheric component contributions, in order to maximize the amount of data used in the analyses. To prevent the masking of surface absorptions and nonlinear mixing of atmospheric components, spectra with dust and ice extinctions >0.25 and >0.15, respectively [*Bandfield et al.*, 2000b], or >0.18 and >0.10 respectively [*Bandfield*, 2002] were excluded. However, the effect of dust and ice contributions on derivation of surface emissivity, at levels below previous constraints, has not been examined in detail.

[26] Surface emissivity for three low-albedo regions (Sinus Meridiani, Syrtis Major and Solis Planum) was derived using data containing varying levels of atmospheric dust

Table 2. TES Data Selection Constraints[a]

	1a	1b	2a	2b	3
Target temperature, K	≥270	≥255	≥270	≥245	≥250
Emission angle	≤30	≤30	≤30	≤30	≤30
Orbit range[b]	1 to 5317	1 to 5317	1 to ~3100	1 to ~3100	1 to 5317
Total ice extinction	≤0.04	≤0.04	opacity ≤ 0.1[c]	≤0.15	≤0.10
Total dust extinction	≤0.15	≤0.15	opacity ≤ 0.3[c]	≤0.25	≤0.18
Lambert albedo	<0.14	<0.15	<0.15	n. a.	n. a.
Image motion compensation	none	none	none	none	none
Scan length (wave number spacing)	10	10	10	10	10
Quality: Solar panel motion[d]	unknown or <0.120 deg/sec	unknown or <0.120 deg/sec	-	-	-
Quality: High gain antenna motion[d]	unknown or <0.05 deg/sec	unknown or <0.05 deg/sec	-	-	-

[a]Constraints given for this study and for two others that are most similar to this one. Not all TES studies are included in this table. Column headings: 1a, this study, spectral shape derivation; 1b, this study, spectral shape distribution; 2a, *Bandfield et al.* [2000b], spectral shape derivation; 2b, *Bandfield et al.* [2000b], spectral shape distribution; 3, *Bandfield* [2002]. A dash means "not given" and "n. a." means "not applicable". Albedo constraints were not used in 2b and 3 because maps were shown as concentrations rather than abundances, along with RMS error. Because concentrations are not normalized for blackbody, surface concentrations over high-albedo regions were naturally low and below the detection limit, therefore an albedo mask was not required.

[b]MGS mapping phase orbit number. To convert to orbit counter keeper (OCK) number, add 1683.

[c]*Bandfield et al.* [2000b] (2a), listed dust and water ice constraints in terms of opacity rather than extinctions. A dust opacity (9 μm) of 0.3 corresponds to dust extinction of ~0.2; an ice opacity (11 μm) of 0.1 corresponds to an extinction of ~0.08.

[d]Additional quality and observational fields from the TES database used in this study: major_phase_inversion 0 0, algor_risk 0 0, spectral_mask 0 0 and detector_mask_problem 0 0. A description of all database fields are listed at http://tes.asu.edu/sourcebook/

and water ice (Figure 1). The spectral library used is given in Table 1. The average spectrum from individual orbits shown for each example cover approximately the same location on the surface.

[27] Figure 1 illustrates that even with levels of atmospheric water ice below constraints used in previous work (Table 2), the derivation of surface emissivity is adversely affected. Within the examples shown, spectra with the highest levels of water ice (extinctions of 0.05–0.06) exhibit a relative increase in surface emissivity between 300 and 380 cm^{-1}, compared to derived surface emissivity from spectra with the lowest amount of water ice (extinctions <0.03). The example with the highest amount of water ice (Meridiani, Figure 1b) also contains a false surface absorption between 980 and 1050 cm^{-1}. The absorption feature is less prominent in the Syrtis Major and Solis Planum examples, suggesting either that its appearance is affected by minor changes in the concentration of water ice in the measured spectrum, or that this feature is not consistently produced from regions with slightly different surface emissivity. The positions of false surface absorptions and increased emissivity could vary for other examples, depending on the true surface emissivity and the potential surface end-members available in the library. On the basis of these three examples, we find that best results are obtained if the level of water ice extinction is limited. If available, examination of multiple orbits over the surface of interest should help to determine if atmospheric components are being properly separated from the surface components.

[28] Levels of atmospheric dust extinctions >0.15 may adversely affect derived surface emissivity. For all three examples, at dust extinctions >0.15, there is an apparent surface absorption between 890 and 930 cm^{-1}, and an overall increase in surface emissivity between 950 and 1050 cm^{-1}. As mentioned above for water ice, effects could vary for other examples depending on the surface emissivity and the spectral library used. Deconvolution of TES spectra with an excessive amount of atmospheric dust (in these examples, dust extinctions > 0.15) may result in derived surface emissivity with false surface spectral features.

3.2. Negative Water Ice Concentrations

[29] Where using the linear deconvolution algorithm for surface-atmosphere separation, the measured emissivity is modeled using positive concentrations of potential surface end-members, and either positive or negative concentrations of atmospheric dust and/or water ice (section 2.2.2). In some cases, we have found that low negative concentrations of water ice are occasionally used in combination with positive concentrations of EPF surface dust to model surface components, even where EPF surface dust is not expected to be a major component (i.e., from a low-albedo surface). Figure 2a shows an example of where this has been observed to occur in northern Acidalia Planitia. Positive concentrations of EPF surface dust are used in combination with negative concentrations of water ice to model a surface component, though TES albedo (0.11) and dust cover index (0.97) [*Ruff and Christensen*, 2002] of this area suggests that surface dust should not be present at high concentrations. However, derived surface emissivity where EPF surface dust is included in the spectral library includes a significant (0.32) modeled concentration of this end-member. When EPF surface dust is excluded, a lower negative concentration of water ice is used in the final solution; therefore the derived surface emissivity shape is not the same. Figure 2b illustrates a suggestion of why this occurs. EPF surface dust may be reasonably well-modeled with other minerals and positive concentrations of water ice. When water ice is excluded, EPF surface dust cannot be modeled well with other spectra in the library. It is possible that EPF surface dust might occasionally be used instead of small concentrations of water ice to model the emissivity spectrum. This would affect the amount of water ice that is subtracted from the measured spectrum. As with the previous example, the degree and frequency of this occurrence is likely dependent on the spectra available in the library. If there is concern that negative water ice concentrations are affecting the derived surface emissivity, water ice end-members may be only allowed in the final solution as positive concentrations (Figure 2a). In the example in Figure 2a, similar surface shapes are produced by

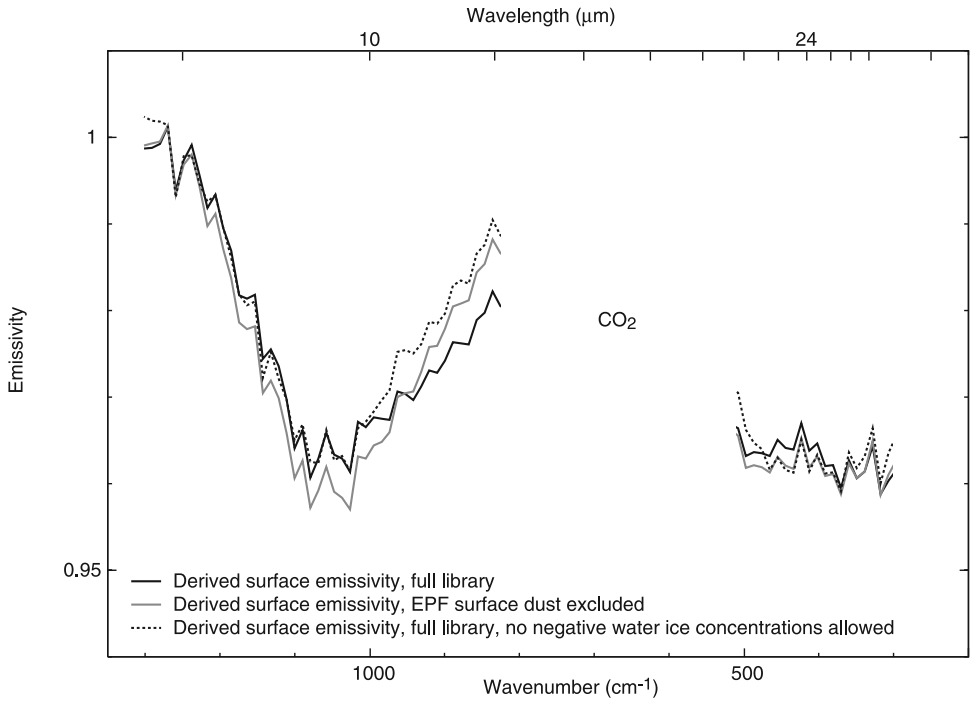

Figure 2a. Effect of negative atmospheric water ice concentrations on derived surface emissivity. Linear deconvolution-derived surface emissivity spectra from Acidalia Planitia. All three spectra are derived from the average of OCK 2619, ICKs 2232–2237. The first spectrum is derived with a mineral and atmospheric end-member library. The second library is the same, but with EPF surface dust excluded. The third library is the same as the first, but water ice end-members were only allowed in positive concentrations. Note the similarity between the surface emissivity shapes (between ~815 and 1300 cm^{-1}) with surface dust excluded and with no negative water ice concentrations allowed.

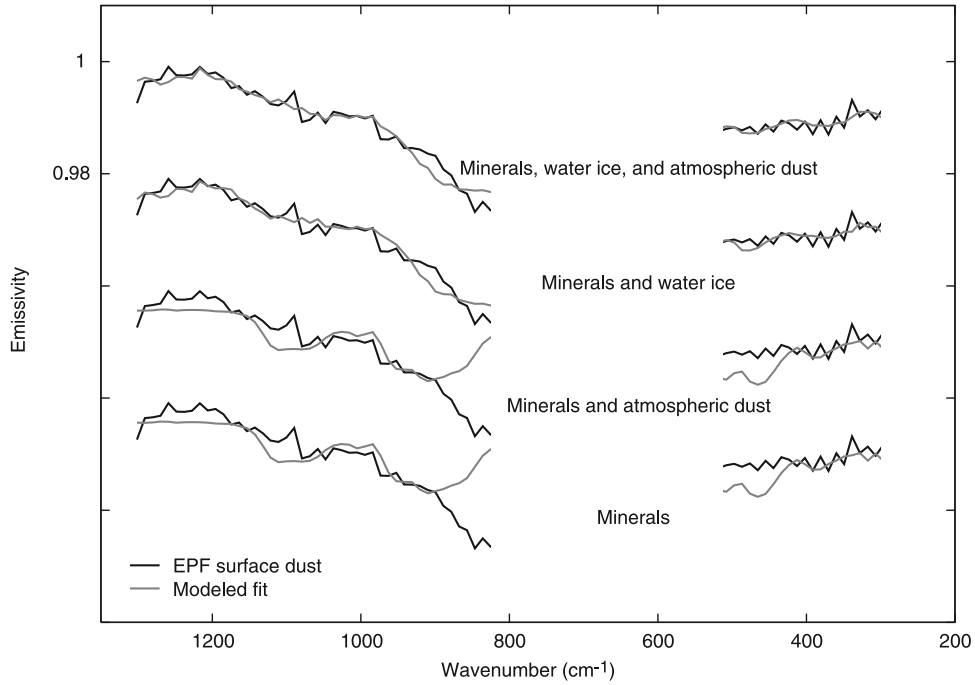

Figure 2b. Model fits to EPF surface dust using the spectral library in Table 1 (EPF surface dust excluded) with (first set of curves) the full library, (second set of curves) atmospheric dust excluded, (third set of curves) water ice excluded, and (fourth set of curves)) atmospheric dust and water ice excluded. Negative concentrations of atmospheric components were allowed in all models. Positive concentrations of water ice were used to model the EPF surface dust in the first and second sets of curves. EPF surface dust is modeled well when positive concentrations of water ice are included.

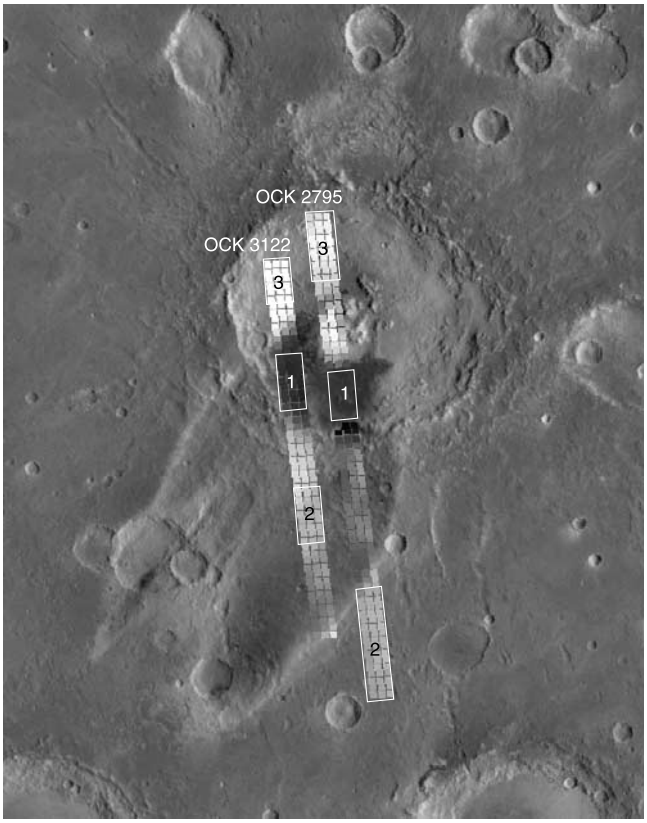

Figure 3a. TES albedo variations observed in OCKs 2795 and 3122 and locations of spectra extracted for Figure 3b. Background image is Viking MDIM 2.0. The area shown is ~13.2°N–19.3°N, ~352.7°E–357.3°E.

(1) excluding EPF surface dust or (2) only allowing positive water ice concentrations. If there is confidence from other information that the surface of interest is relatively free of dust (i.e., from short-wavelength emissivity [*Ruff and Christensen*, 2002] or albedo), the EPF surface dust spectrum may be excluded.

3.3. Low Surface Spectral Contrast

[30] To examine the effect of low surface spectral contrast on derived surface emissivity using the linear deconvolution method, we used TES data from two orbits that traversed low- and high-albedo surfaces within and around Radau crater (Figure 3a) (following *Johnson et al.* [2002b]). Figures 3b and 3c show effective emissivity spectra taken from surfaces with TES albedo values of 0.11 and 0.21–0.27. In these examples, the largest difference between the bright and dark surfaces should be due to spectral contrast; differences due to atmospheric components should be minimal.

[31] Accurate surface-atmosphere separation of spectra from bright surfaces using the linear deconvolution method should produce a shape similar to the globally uniform EPF surface dust shape [*Bandfield and Smith*, 2003] (section 2.2.1). Figures 3d and 3e show surface emissivity derived for each spectrum in Figures 3b and 3c using the spectral library in Table 1. The derived spectra of the low-albedo crater floor material (~0.11) are typical of basalt, as expected. However, the linear deconvolution-derived emissivity spectra from the high-albedo surfaces are not good matches to EPF surface dust (Figure 4). These examples indicate that the linear deconvolution method may not always properly remove atmospheric components from spectra of higher-albedo surfaces ($\geq$0.20).

[32] The Radau Crater spectra may also be used to discuss systematic end-member use and model fits to spectra from high-albedo regions. Model fits to the Radau Crater spectra worsen with increasing albedo (Figures 3d and 3e). This is observed globally [*Bandfield*, 2002]: RMS error increase becomes most prominent over regions that exhibit average 9–10 μm emissivity > ~0.96–0.97 (Figure 5). For the high-albedo surfaces (>0.20) in Figure 3, high-silica phase(s) are used to model the spectra, along with alkali feldspar, sulfates, and EPF surface dust. Pyroxene is not used. Results for these examples are consistent with global mineral maps derived by *Bandfield* [2002, 2003], which show that coarse-particulate sheet silicates/high-silica glass, K-feldspar, and sulfates are used in addition to EPF surface dust to model surface emissivity over parts of the classic high-albedo regions of Tharsis, Arabia and Elysium. This suggests that high-silica phase(s), feldspar and/or sulfates are systematically and erroneously used by the linear least squares fitting algorithm to model emissivity from the lowest spectral contrast regions.

[33] For intermediate albedo (0.15–0.19), intermediate spectral contrast surfaces (we note that albedo is not necessarily indicative of spectral contrast), where surface emissivity has not yet been confirmed through other means, it is difficult to assess the accuracy of the linear deconvolution surface-atmosphere separation method. It is not clear what minimum spectral contrast is required for reliable surface emissivity retrieval using this technique; however, derived surface emissivity probably does become less certain as the contrast of surface spectral features is decreased.

3.4. Summary

[34] In summary, if linear deconvolution is used to determine surface emissivity, multiple orbits should be examined, if available. Additional techniques (section 2.2) may also be used to build confidence in the derived surface shapes. Water ice and dust extinctions above 0.04 and 0.15, respectively, may adversely affect derived surface emissivity. In addition, negative concentrations of water ice are occasionally used in combination with EPF surface dust to provide the best fit to the measured spectrum, even when dust is not a likely component of the surface. Finally atmospheric components may not be accurately separated from surfaces with low spectral contrast. High-silica phases, feldspar and/or sulfates are commonly used to model the emissivity of low spectral contrast regions. Finally, as the relative contribution from the surface component to measured spectrum is decreased, reliability of the derived surface emissivity is likely diminished (sections 2.2.2 and 3.3).

4. Approach

4.1. Overview

[35] Mineral mapping is one method for determining spatial variations in mineral abundance, however it is

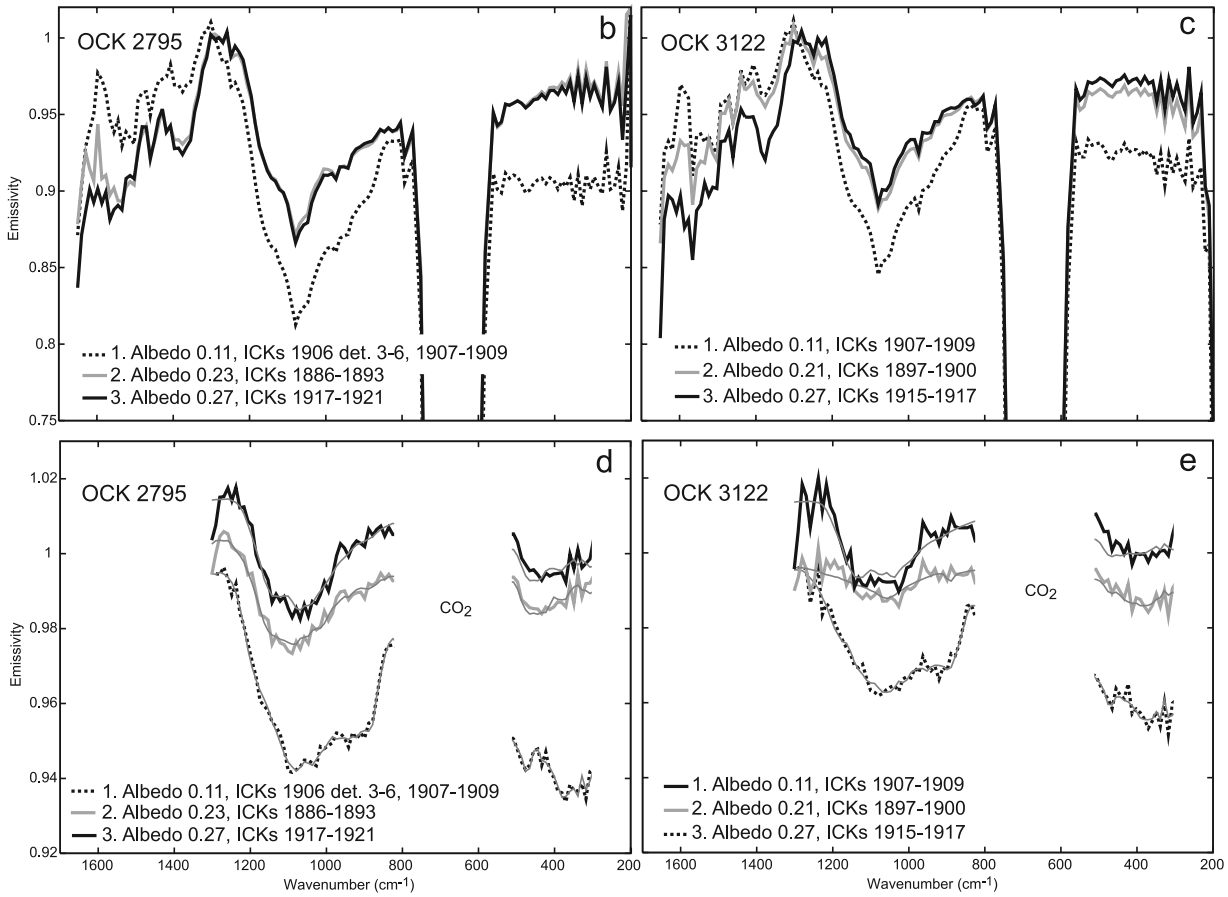

Figure 3b–e. (b, c) Average effective emissivity spectra from surfaces of varying albedo from OCKs 2795 (Figure 3b) and 3122 (Figure 3c). (d, e) Surface emissivity derived from spectra in Figures 3b and 3c, using the linear deconvolution method. No contrast enhancement was applied. Spectrum 2 in both plots was offset by 0.01 for clarity. The derived spectra of the low-albedo crater floor material (spectra numbered 1) is typical of basalt.

difficult to visualize how an assemblage of minerals with constant relative mineral abundance (example: clinopyroxene + plagioclase + olivine) varies together spatially. This kind of visualization is important for relating bulk surface mineralogy to other crustal properties, such as surface morphology/age or crustal thickness. The approach of using "spectral unit types," such as that of *Bandfield et al.* [2000b] allows the user to classify a particular phase assemblage by its characteristic spectral shape, and then determine the distribution of that assemblage. In this work, 29 low-albedo regions were selected in an effort to sample the global diversity in surface age, crustal thickness, latitude and elevation (Figure 6). Note that the low-albedo hematite-rich region in Meridiani Planum was excluded from this study. For each area, a regional surface emissivity shape was derived from individual TES orbits. These regional shapes were then grouped by similarity to produce eleven representative low-albedo region spectra, and the global distributions of each representative spectrum were determined. Surface emissivity shapes were validated using spectral ratios (where appropriate conditions were available) and comparison of non–atmospherically corrected spectra from individual orbits that cross spectrally different regions.

4.2. Data Selection and Reduction

[36] Both binned emissivity data and individual orbit tracks are used in this work. Individual orbit tracks are used to derive the average surface spectral shape for each low-albedo region. For this step, the TES data used was limited to MGS mapping orbits 1-5317, dust extinctions <0.15, ice extinctions <0.04, surface temperature >270 K (more than 80% of spectra used were >280 K), solar panel motions unknown or <0.120 deg/sec, HGA motions unknown or <0.05 deg/sec, and emission angles <30° (Table 2). Note that the allowable water ice concentrations in this study are significantly lower than previous studies (Table 2), because this work focuses on areally extensive regions where there is sufficient data available that meet these limited constraints. The solar panel and HGA movement constraints were used in an effort to avoid orbits containing spectral artifacts [e.g., *Bandfield*, 2002; *Hamilton et al.*, 2003b], however it should be noted that these constraints do not completely eliminate all of the spectra containing artifacts. In this step of deriving the regional spectral shapes, all spectra were manually examined to ensure the absence of artifacts. Emissivity spectra binned at a spectral resolution of 1 pixel-per-degree are used to determine the distribution of representative low-

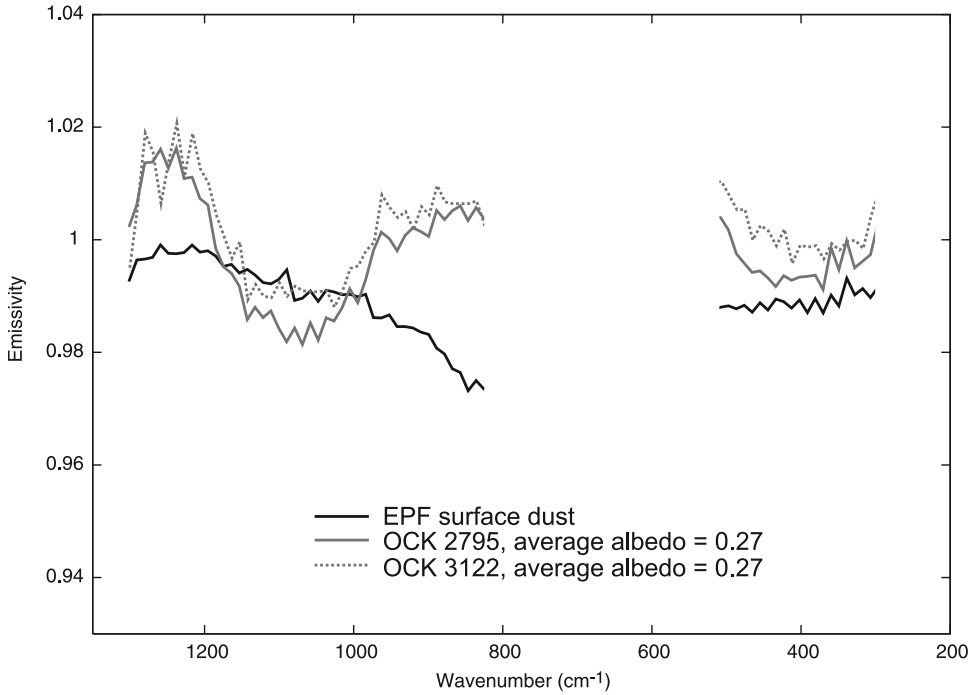

Figure 4. Comparison of high-albedo linear deconvolution-derived surface emissivity spectrum from Figure 3c with EPF surface dust. No offset or contrast enhancement was applied.

albedo surface spectral shapes. For the binned data, TES data set queries are similar to those used for individual orbits, except that surface temperatures as low as 255 K were allowed to provide increased spatial coverage. Spectra from colder surfaces have a lower signal-to-noise ratio than spectra from warmer surfaces, however, several spectra (at least 50, but usually >100) are averaged per bin, which improves the signal. Similarly, the influence of any artifacts

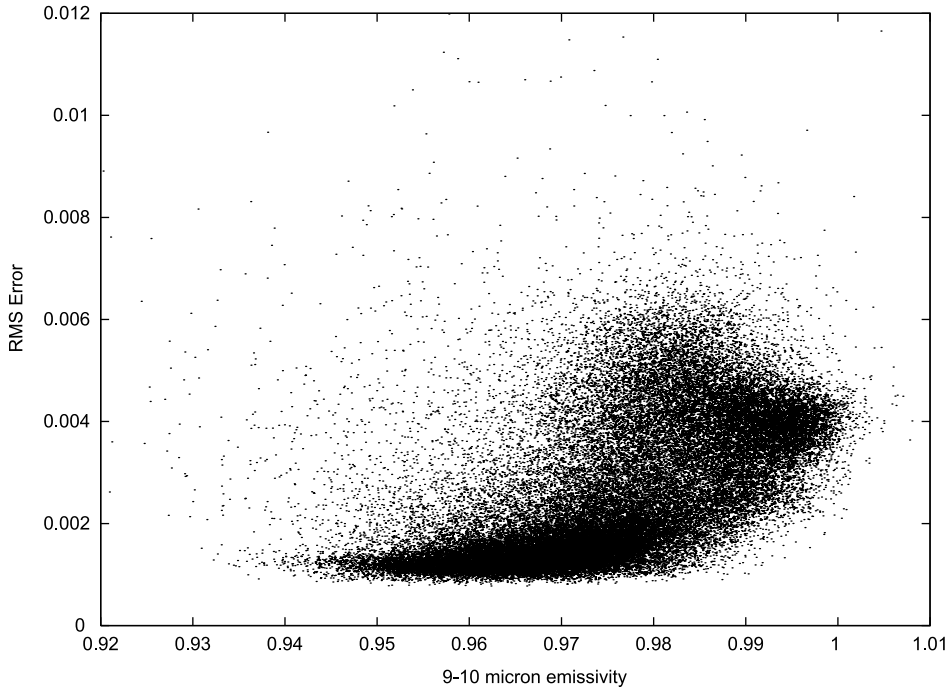

Figure 5. RMS error from *Bandfield* [2002] versus spectral contrast of surface emissivity derived from *Bandfield* [2002]. The average surface emissivity between ~9 and 10 μm is used as a gauge of spectral contrast. As the ~9–10 μm emissivity increases to >~0.96–0.97 (decreasing spectral contrast), a noticeable increase in RMS error for modeled spectra occurs.

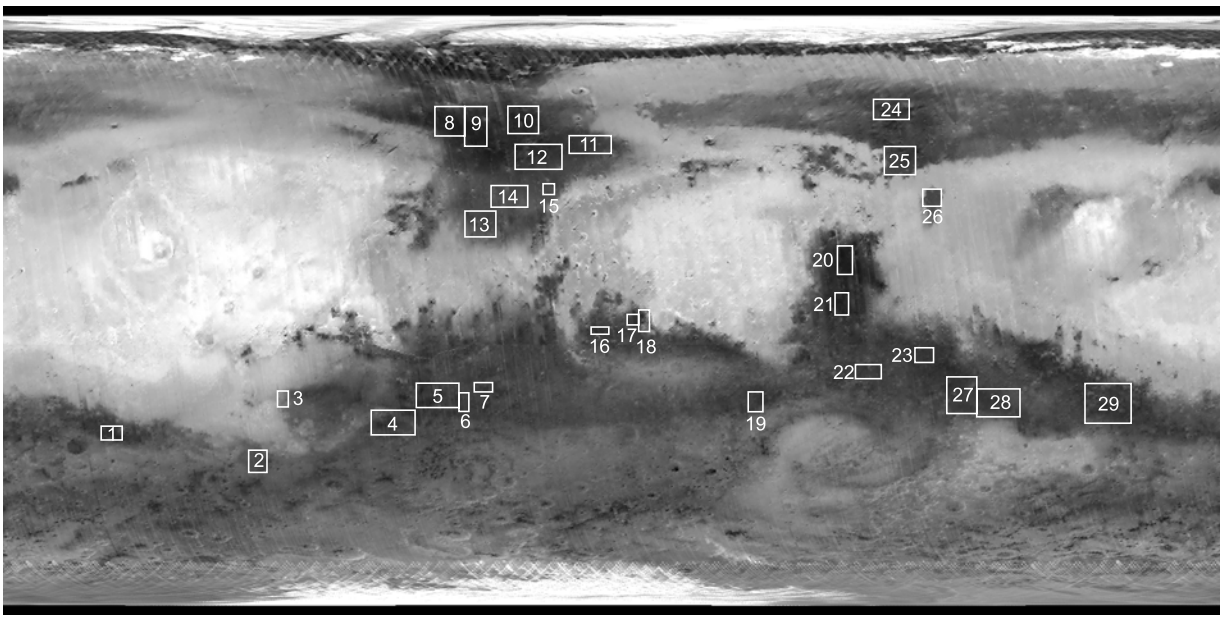

Figure 6. Global TES albedo map, centered at 0° longitude, showing locations of the 29 low-albedo regions in this study. Numbers correspond with numbered region names in Table 3.

present in the binned data is mitigated by averaging spectra from several orbits per bin. Finally, all spectral fitting was limited to ~307–1301 cm^{-1}, excluding the atmospheric CO_2 region between ~518 and 815 cm^{-1}.

4.3. Regional Spectral Shape Derivation

[37] Using the data set constraints above, the locations of individual orbit tracks were mapped for each region (example, Figure 7). For each orbit, a range of ICKs covering surfaces with TES lambert albedo values $\leq$0.14 with similar atmospheric contribution (Figure 8) was selected and averaged (Table 2). Because there are hundreds of spectra that meet the data constraints discussed above, we chose to use an albedo upper limit of 0.14 (as opposed to 0.15) in this step of our approach in an effort to derive the regional spectral shapes from the best possible surface conditions (e.g., highest spectral contrast and warmest surface temperatures). One exception to the albedo constraint was the southwest Solis Planum region, which has an average albedo of ~0.16–0.17. This region was included because it was already shown by *Bandfield* [2002] to have deep spectral contrast; in addition, despite the higher albedo, the dust cover index [*Ruff and Christensen*, 2002] for this region (0.96–0.99) is similar to lower albedo regions. Atmospheric components were removed from the average spectrum using the linear deconvolution method. The spectral library used to fit the measured spectrum is given in Table 1. In this step of deriving representative surface shapes, we chose to exclude EPF surface dust, because only spectra from the lowest albedo surfaces were used. This was done to avoid rare cases of false combination of negative water ice concentrations with positive EPF surface

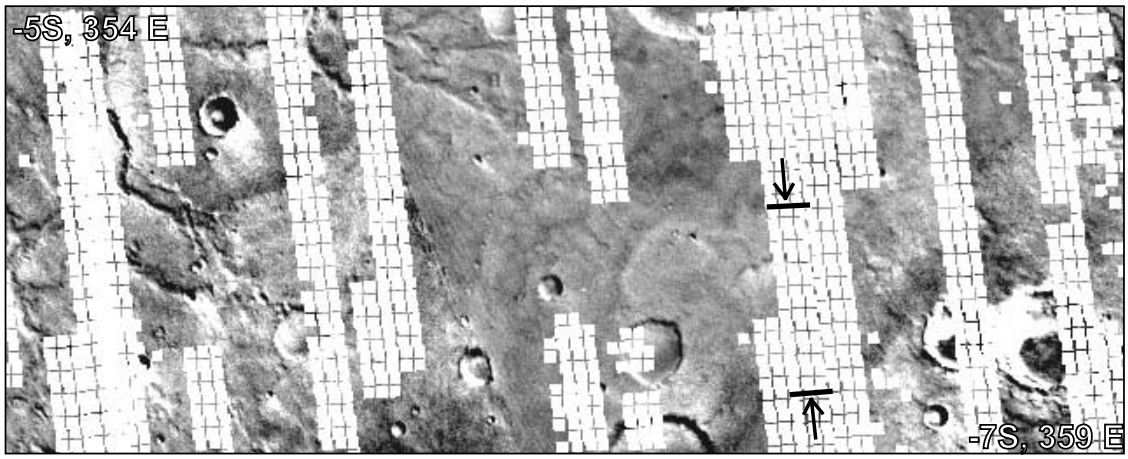

Figure 7. Examples of TES data coverage using constraints listed in section 4.2. The region shown is box 16, Sinus Meridiani. Black arrows point to spatial locations of spectra shown in Figure 8.

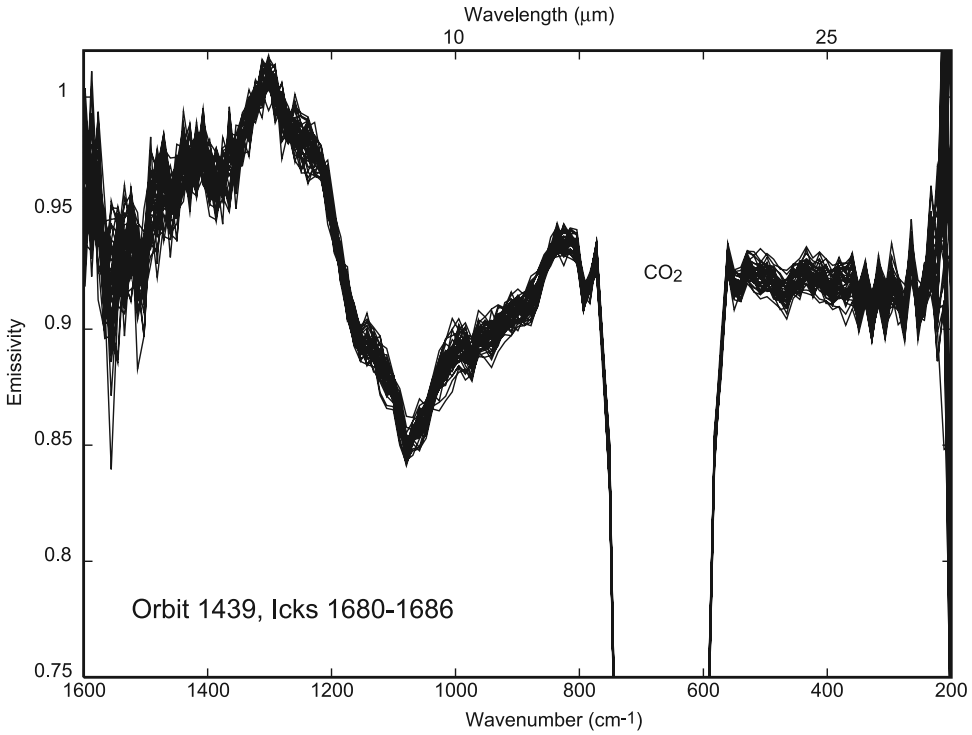

Figure 8. Example of the worst-case level of spectral variability that was allowed when averaging spectra from each individual orbit (for derivation of each regional shape). Spectra are from Sinus Meridiani, region 16, TES mapping phase orbit 1439, ICKs 1680–1686 (location indicated with arrows in Figure 7).

dust concentrations (section 3.2). Surface emissivity shapes derived from each orbit were normalized to the average spectral contrast and plotted for comparison (Figure 9). The most recurrent surface shapes within the set of spectra were selected and averaged to produce the regionally dominant surface emissivity shape. In most cases, the number of orbits used for each representative shape was greater than 90% of the available orbits. For two of the regions (Syrtis Major and southern Acidalia), only 65% of the available orbits were used. Orbit-to-orbit and along-track variations were observed in the derived surface shapes for these regions; most of this variation is likely due to real surface variation in mineralogy or dust coatings, whereas a small percentage could be due to influence from atmospheric water ice or dust (section 3.1).

4.4. Global Spectral Shape Classification

[38] The regional spectral shapes derived for each of the 29 low-albedo areas were scaled to their average spectral contrast and plotted for comparison. If two or more shapes from different regions were similar, the shapes were combined by taking both sets of spectra and averaging them together to produce a representative spectrum. Regional shapes were considered dissimilar if the average was not within the standard deviation associated with all other shapes, over a $\geq$50 cm^{-1} range. Using this criterion, error bounds do overlap for a few of the shapes, and differences between some of the shapes are subtle. However, the spatial contiguity that is apparent when mapping the distribution of these shapes (section 5.2) supports the separation criterion used. If a more stringent separation measure is used, then spectral detail that is mappable in coherent distributions across the planet is lost. In addition, the act of combining the spectra with only subtle differences presumes that the differences are not due to real surface properties, which is not ideal. In Paper 2, the most similar spectra in this work are ultimately recombined on the basis of comparable mineralogy. The method presented here and in Paper 2 of mapping spectral details, and then recombining the distributions of similar spectra on the basis of mineralogy, results in more distinct compositional distributions without overinterpreting the subtle differences between these spectral shapes as representing extreme differences in surface mineralogy or physical effects.

4.5. Spectral Shape Distribution

[39] The representative low-albedo region spectral shapes described above and previously derived atmospheric end-members [*Bandfield et al.*, 2000a; *Bandfield*, 2002] were used to deconvolve effective emissivity spectra binned at a resolution of 1 ppd from 70°S to 70°N. Owing to the global nature of this study and the use of binned data to derive maps, surface dust was not excluded from this step, and negative water ice concentrations were allowed. The output of the model includes maps of spectral shape concentrations and RMS error. This approach is similar to that of *Bandfield* [2002] (section 2.3.2), except that representative surface spectral shapes are used as potential surface end-members instead of minerals and glasses.

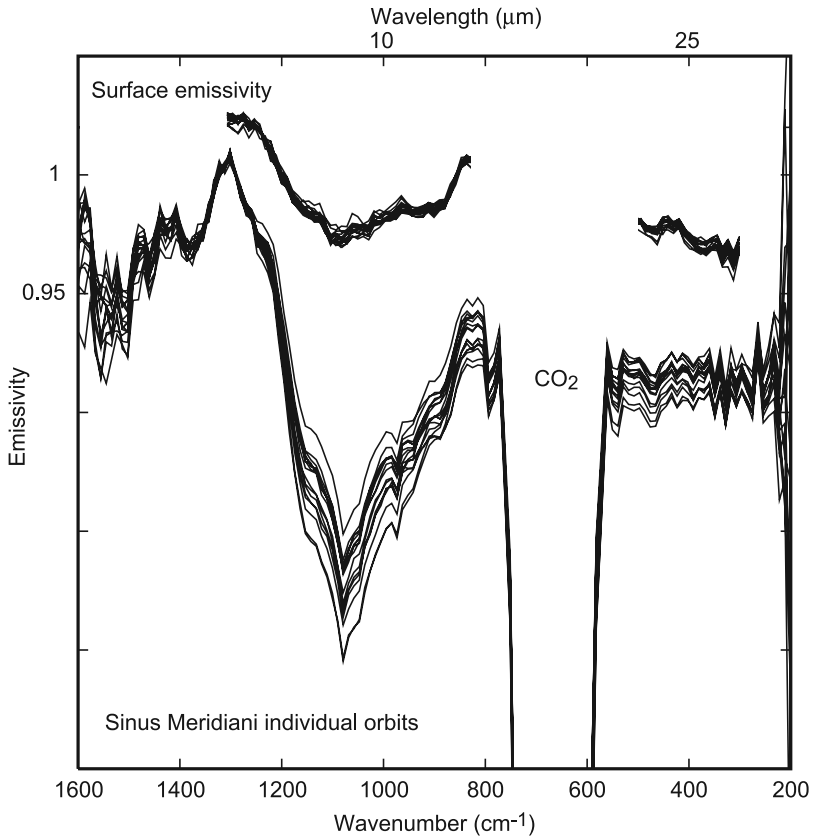

Figure 9. Example of how representative regional surface emissivity shapes are derived. Each spectrum in the lower set is the average of 50–300 spectra from a single orbit in the Meridiani region (areas 16–18, Table 3). Note variability in atmospheric dust (prominent absorption between ~850 and 1200 cm^{-1}) within this set of spectra. Each spectrum in the upper set is the derived surface emissivity from the lower set. The derived surface emissivity shapes are normalized to the average spectral contrast.

4.6. Corroborative Methods

[40] The initial and perhaps most robust check on the validity of the derived regional surface shape is if a consistent surface spectrum is obtained from orbits with varying levels of atmospheric contributions (Figure 9). In addition, where possible, spectral ratios were used to verify the spectral shapes. An example of this is given in Figure 10. TES spectra were selected from a single orbit that crossed the surface of interest and a nearby brighter region. As mentioned above, the surface emissivity of bright regions is well constrained (EPF surface dust) [*Bandfield and Smith*, 2003; *Christensen et al.*, 2004a]. The surface of interest is an area that is mapped as a particular representative shape (in this example, Cimmeria Terra is mapped as the Cimmeria-Iapygia spectral shape). If the representative surface emissivity shape was correctly derived using the linear deconvolution method, then the ratio spectrum of the dark surface divided by the bright surface should match a ratio of the representative surface emissivity spectrum divided by EPF surface dust [*Ruff and Christensen*, 2002]. However, for almost all of the regions of interest in this study, there was rarely a high-albedo surface (>0.20) in close enough proximity to the surface of interest. Instead, we commonly used adjacent areas that were slightly brighter than the dark region of interest to create a spectral ratio (Figure 10a), and assumed that the adjacent brighter surface was a mixture of the dark material of interest and EPF surface dust. High wave number (>1350 cm^{-1}) features in the ratio spectrum of a dark region and adjacent brighter region with similar substrate composition should be due primarily to differences in dust abundance. To determine the fractional contribution of dust to the brighter region, the magnitude of spectral features at high wave numbers (1350–1600 cm^{-1}) in the ratio spectrum was compared to the magnitude of spectral features in the EPF surface dust spectrum (Figure 10b). Finally, the representative spectral shape was divided by the EPF surface dust spectrum [*Bandfield and Smith*, 2003], scaled by the determined percentage of contribution, for comparison to the ratio spectrum (Figure 10c).

[41] Areas that meet the ratioing criteria (section 2.2.3) are limited; therefore only one example is given for each representative low-albedo region shape derived in this work. In addition, some of the shape distributions did not have distinctly brighter surfaces in close enough proximity to the surface of interest, therefore not all representative shapes were able to be verified by this method. In two of these cases, we used visual inspection of non–atmospherically corrected spectra from single orbit tracks that cross spectrally different regions for changes in the 300–500 cm^{-1} spectral region (where atmospheric components are the

most transparent) as a method of confirming spectral differences between regions.

5. Results

5.1. Regional Spectral Shapes

[42] Eleven average spectral shapes are shown in Figure 11, and are representative of the spectral response from the 29 low-albedo regions studied (Table 3). The non–atmospherically corrected emissivity spectra from individual orbits used to derive each representative spectral shape are shown in Figure 12. For each region (with the exception of Pandorae), varying amounts of atmospheric dust are present within the set of orbits used to derive the regional surface shapes. The fact that the uniform surface emissivities were derived from spectra with widely varying dust opacities provides the best indication that atmospheric components have been correctly removed and other effects are not present. Less confidence is associated with the Pandorae Fretum shape because there is little atmospheric variation between the orbits used to derive the shape. All derived spectral shapes are generally similar to each other, with broad absorptions between ~850–1300 cm^{-1} and ~300–500 cm^{-1}. However, there are significant, though subtle, differences.

5.2. Notable Features and Global Distributions of Spectral Shapes

[43] Representative spectral shape concentration maps are shown in Figure 13. Map areas with clear-period TES albedo values (derived by *Christensen et al.* [2001]) >0.15 are masked out, with the exception of the Solis Planum spectral shape distribution map, where surface albedo values up to 0.17 are included. Most of the concentration maps are spatially coherent although the differences between the eleven shapes are subtle (Figure 11). Spatial contiguity adds additional confidence that the spectral variations are not due to artifacts or atmospheric effects. The distributions of the representative spectral shapes are described in detail below.

[44] The spectral shape that is representative of low-albedo regions in southern Acidalia has a slightly lower spectral contrast than the other regional shapes. The shape is remarkably similar to that derived by *Moersch et al.* [1997] for Acidalia Planitia using telescopic observations. There is some surface variability as evidenced by the percentage of orbits (~65%) used to derive the shape. High concentrations of this spectral shape are found primarily in southern and eastern Acidalia Planitia, as well as a few areas in southern Utopia Planitia. These regions are slightly higher albedo (~0.13–0.15) than the other dark regions of this study, which is consistent with the slightly lower spectral contrast of the southern Acidalia representative shape. We note that lower concentrations of this spectral shape are used in addition to EPF surface dust to model surface emissivity from the higher-albedo regions (>0.15). These

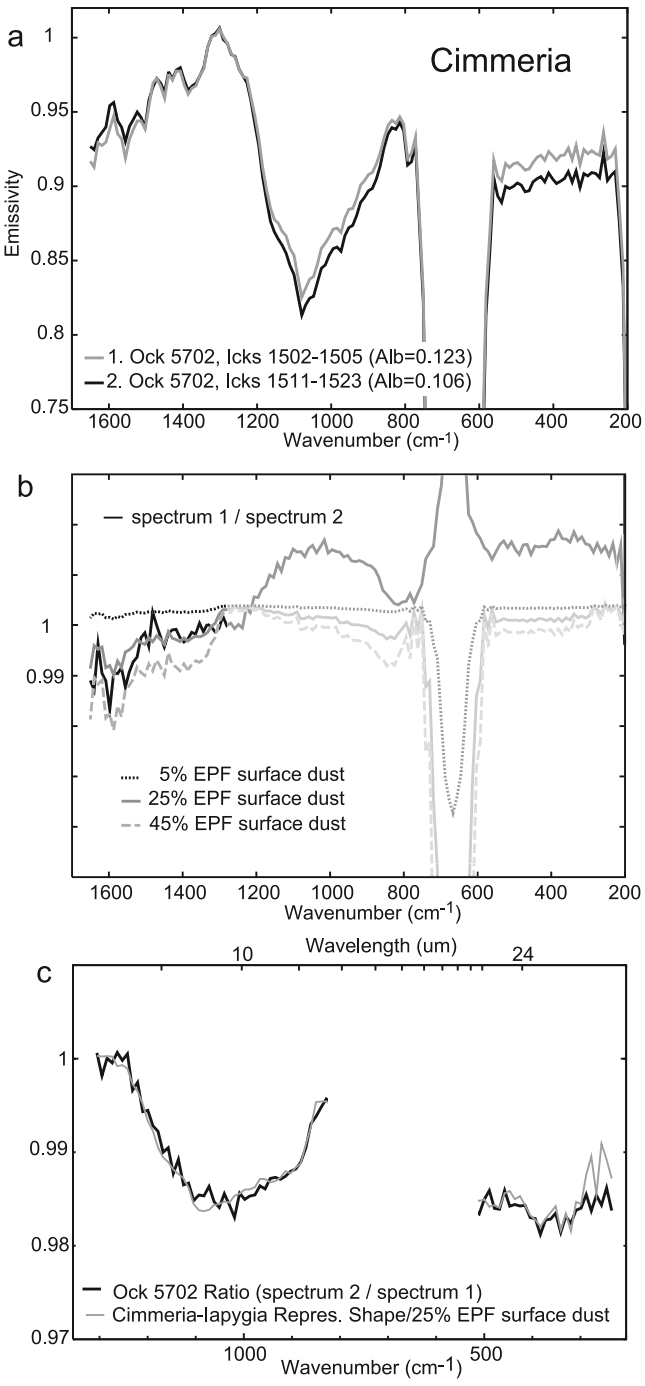

Figure 10. Example of how spectral ratios are used to verify surface emissivity derived from linear deconvolution. (a) TES effective emissivity spectra from OCK 5702 in Cimmeria Terra. The lower spectrum is from the region of interest, and the upper spectrum is from an adjacent region with more surface dust. Spectral differences are due primarily to differences in surface dust abundance and spectral contrast. (b) Ratio of spectra from Figure 10a, compared with the EPF surface dust spectrum, scaled at abundances of 5, 25, and 45%. An abundance of 25% gives the best match to the short wavelength (1350–1600 cm^{-1}) emissivity features of the ratio spectrum. (c) The ratio of spectra from Figure 10a, compared with the Cimmeria-Iapygia-Protei representative shape divided by 25% EPF surface dust. The match indicates that the linear deconvolution derived surface emissivity spectrum for Cimmeria Terra is corroborated by spectral ratios of non–atmospherically corrected spectra.

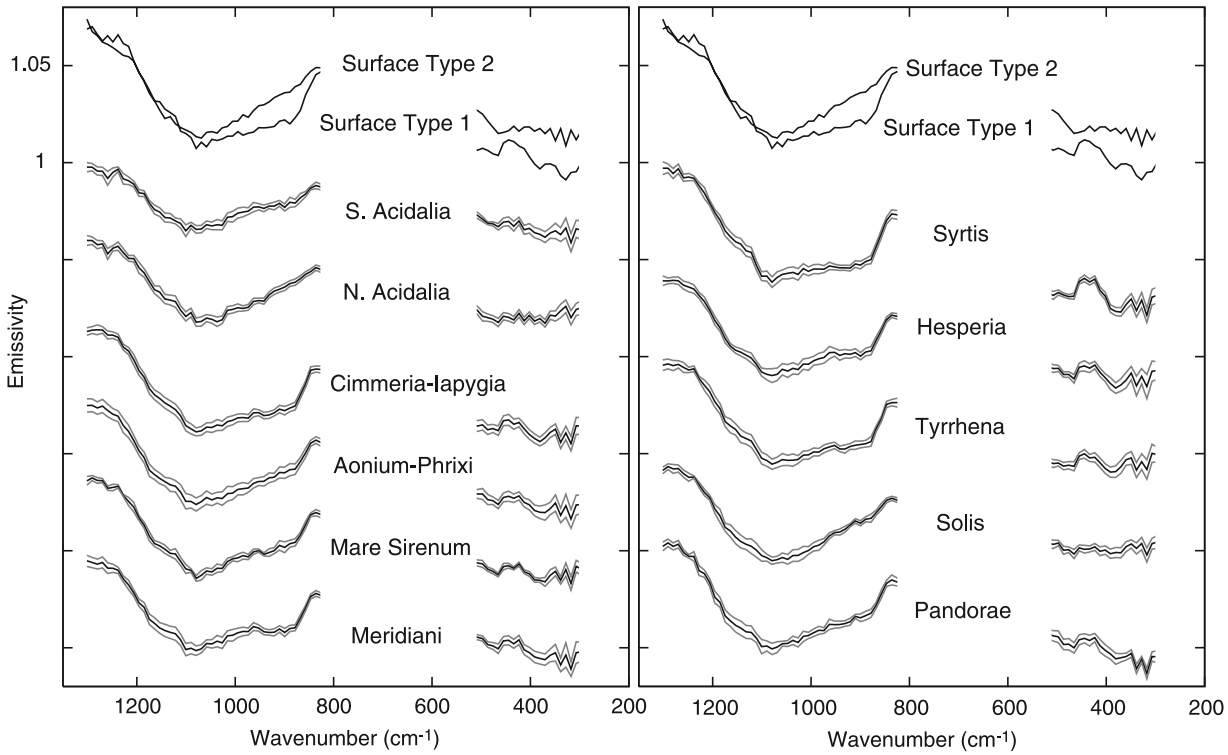

Figure 11. Representative surface emissivity shapes from the 29 low-albedo regions studied. Table 3 indicates which regions were classified into each representative surface emissivity group. Gray lines represent the standard deviation for each average spectrum. Spectra are offset for clarity and shown compared to the global Surface Type 1 and Type 2 end-members [*Bandfield et al.*, 2000b]. No contrast enhancement was applied.

Table 3. Locations and Names of Low-Albedo Regions

Region	Albedo Feature Name	Common Region Name	Bounding Coordinates	Surface Emissivity Group
1	Mare Sirenum	Terra Sirenum	208–215E, 34–39S	Mare Sirenum
2	Aonium Sinus	Icaria Planum	253–258E, 42–48S	Aonium-Phrixi
3	E. Solis Lacus	E. Solis Planum	261–264E, 24–28S	Solis
4	Phrixi Regio	Bosporos Planum	288–301E, 30–37S	Aonium-Phrixi
5	Protei Regio	na	302–315E, 21–30S	Cimmeria-Iapygia
6	Protei Regio	na	315–318E, 25–31S	Cimmeria-Iapygia
7	Mare Erythraeum	Margaritifer	319–325E, 21–24S	Cimmeria-Iapygia
8	Mare Acidalium	Acidalia Planitia	308–317E,52–60N	N. Acidalia-Utopia
9	Mare Acidalium	Acidalia Planitia	317–321E, 49–60N	N. Acidalia-Utopia
10	Mare Acidalium	Acidalia Planitia	330–339E,52–60N	N. Acidalia-Utopia
11	Mare Acidalium	Acidalia Planitia	348–360E, 47–52N	N. Acidalia-Utopia
12	Mare Acidalium	Acidalia Planitia	332–345E,42–49N	N. Acidalia-Utopia
13	Niliacus Lacus	Acidalia Planitia	317–325E,22–29N	S. Acidalia
14	Niliacus Lacus	Acidalia Planitia	324–335E,31–37N	S. Acidalia
15	Niliacus Lacus	Acidalia Planitia	340–343E,34–37N	S. Acidalia
16	Sinus Meridiani	Sinus Meridiani	354–359E, 5–7S	Meridiani
17	Sinus Meridiani	Sinus Meridiani	5–8E, 1–4S	Meridiani
18	Sinus Meridiani	Sinus Meridiani	8–11E, 0–6S	Meridiani
19	Pandorae Fretum	na	40–45E, 24–30S	Pandorae
20	Syrtis Major	Syrtis Major	67–71E, 11–19N	Syrtis
21	Syrtis Major	Syrtis Major	66–70E, 1S–5N	Syrtis
22	Iapygia	Iapygia	72–80E, 16–20S	Cimmeria-Iapygia
23	NW Mare Tyrrhenum	Tyrrhena Terra	90–95E, 11–15S	Tyrrhena
24	Copais Palus	Utopia Planitia	78–88E, 57–63N	N. Acidalia-Utopia
25	Copais Palus	Utopia Planitia	81–89E, 40–48N	S. Acidalia
26	Alcyonius	Utopia Planitia	92–97E, 31–36N	S. Acidalia
27	Mare Tyrrhenum	Hesperia Planum	99–109E, 20–30S	Hesperia
28	Mare Tyrrhenum	Hesperia Planum	108–120E, 23–31S	Hesperia
29	Mare Cimmerium	Cimmeria Terra	141–154E, 22–33S	Cimmeria-Iapygia

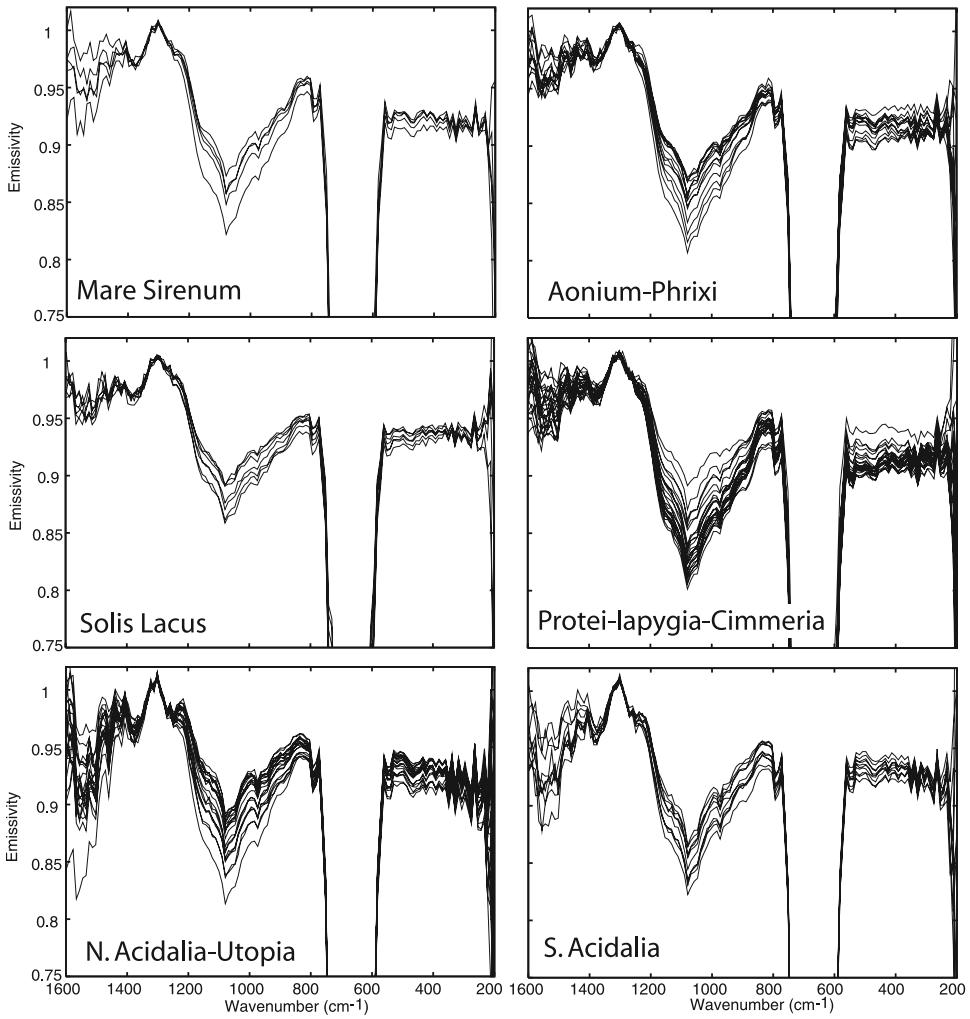

Figure 12. Effective emissivity spectra used to produce the eleven representative regional shapes. Each spectrum within each plot represents an average of 50–300 consecutive spectra from a single orbit. All of the regions (except for Pandorae) have spectra from varying atmospheric conditions that were used to produce the representative shape.

areas are not shown in the albedo-masked concentration maps in Figure 13.

[45] The northern Acidalia representative shape is the most similar to the Surface Type 2 (Acidalia Type) endmember of *Bandfield et al.* [2000b]. The spectral concentration map shows that the northern Acidalia representative shape is confined to northern Acidalia and Utopia, above ~50°N. A spectral and overall visible reflectance difference between northern and southern Acidalia was also apparent in Hubble Space Telescope (HST) 1999 visible [*Farrand et al.*, 2000] and 1997 near-infrared observations [*Noe Dobrea et al.*, 2003].

[46] The Cimmeria-Iapygia spectral shape occurs primarily in the southern highlands, in Protei Regio, Margaritifer Sinus, Iapygia, Mare Cimmeria, and near the western boundary of Hesperia Planum near Tyrrhena Terra. Of the eleven shapes, the Cimmeria-Iapygia concentration distribution is the least spatially coherent and it does not appear associated with any particular type of terrain. This shape may be most representative of the southern highlands of Mars in general. The Cimmeria-Iapygia shape of this work compares well with spectral shapes previously derived for Cimmeria Terra using both radiative transfer and linear deconvolution methods [*Smith et al.*, 2000a].

[47] The Aonium-Phrixi representative spectral shape is largely confined to Hesperian plains surrounding the southeastern section of the Tharsis province. Spatially coherent high concentrations are found in eastern Solis Planum, Phrixi Regio, Thaumasia Planum, and Aonium Sinus. There are a few lower concentrations found near the eastern edge of Acidalia Planitia and Pandorae Fretum.

[48] High concentrations of the Mare Sirenum representative spectral shape are found only in the Mare Sirenum low-albedo region at ~−35°S, 210°E. The highest concentrations are confined mostly to Hesperian-aged plains.

[49] The Sinus Meridiani representative spectral shape is found in high concentrations in Sinus Meridiani (meaning low-albedo surfaces outside of the hematite unit of Meridiani Planum), as well as in Sinus Sabaeus to the east and Margaritifer Sinus and Mare Erythraeum to the west. Other, scattered concentrations are found throughout the southern highlands.

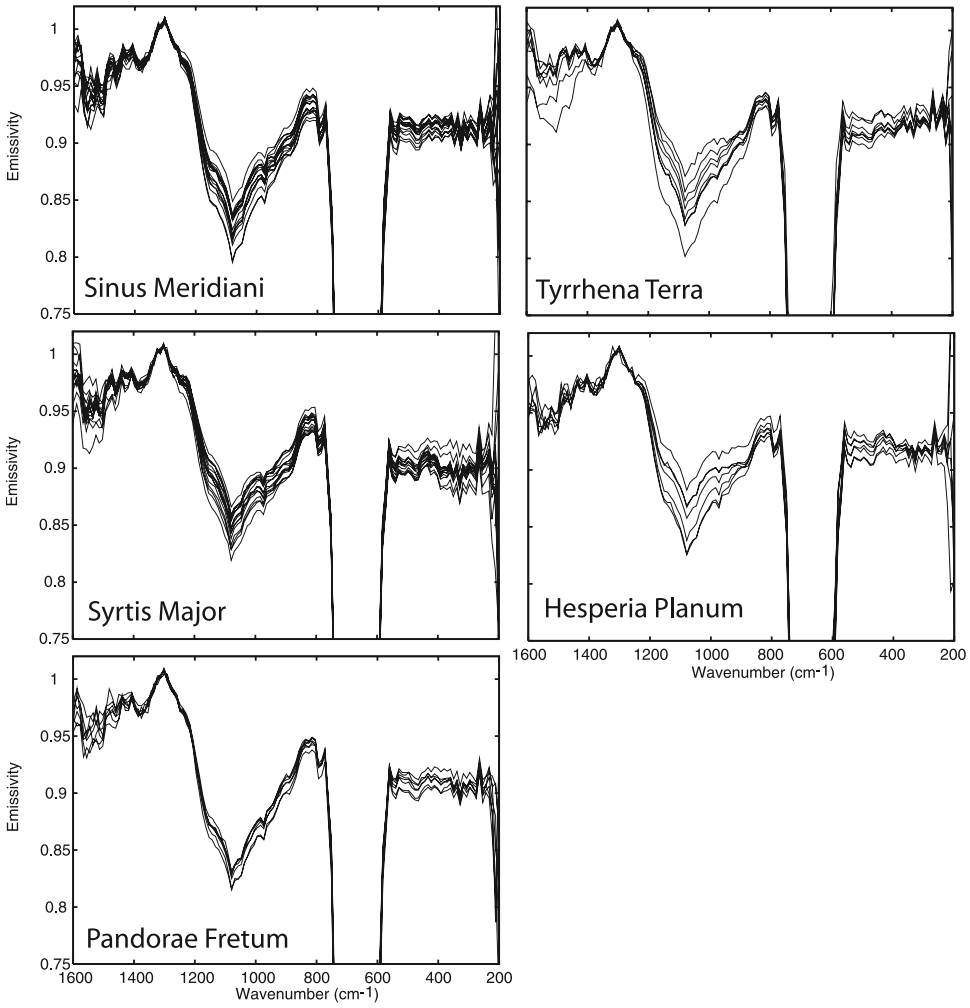

Figure 12. (continued)

[50] The Syrtis Major representative shape is unique to the Syrtis Major province. The derived surface emissivity has higher spectral contrast, and has lower relative emissivity at ~900 cm^{-1} than the Surface Type 1 end-member [*Bandfield et al.*, 2000b]. Only 65% of the available valid orbits were used to produce the dominant shape, indicating some surface variability within Syrtis Major. Spectra not included in the Syrtis Major average deviated more than 15% over >100 cm^{-1} range.

[51] The Hesperia representative spectral shape is found primarily in the dark portions of Hesperia Planum, as well as on the southwestern outermost flanks of Syrtis Major, and Protei Regio. Significant concentrations are also found scattered throughout Iapygia and Cimmeria.

[52] The Tyrrhena Terra representative spectral shape is found primarily (~75%) in Noachian heavily cratered terrains surrounding Hesperia Planum and south of Syrtis Major. There are a few scattered concentrations throughout the Margaritifer Sinus region.

[53] The Solis Planum representative spectral shape is found primarily in the western Solis Planum region, and is similar in spectral character to northern Acidalia (also noted by *Bandfield* [2002]). Low-to-intermediate concentrations are found scattered throughout the southern highlands and in spatially coherent concentrations near the southeastern boundary of the Tharsis province. The primary location of high concentrations in western Solis Planum has a slightly higher average albedo (~0.16) than other regions of this study, however, the dust cover index values (>0.96) [*Ruff and Christensen*, 2002] and surface spectral contrast are similar to the other low-albedo regions.

[54] The highest concentrations of the Pandorae Fretum representative spectral shape with spatial coherence are found in the Pandorae Fretum/Mare Serpentis region, north and northwest of Hellas Basin. Intermediate to low concentrations are found scattered throughout the southern highlands, particularly in Iapygia, south of Mare Cimmerium, and in northwest Syrtis Major.

5.3. Surface Emissivity Shape Validation

[55] As mentioned above, the representative spectral shapes were derived from widely varying atmospheric dust opacities, indicating that atmospheric components have been removed properly (Figure 12). Additional confidence in the derived representative spectral shapes comes from spectral ratios and individual orbits that transition spectrally different areas in the concentration maps. For Syrtis, Pandorae, Protei, Mare Sirenum, Tyrrhena, Aonium, and Meridiani, spectral ratios are shown in Figure 14. Areas with

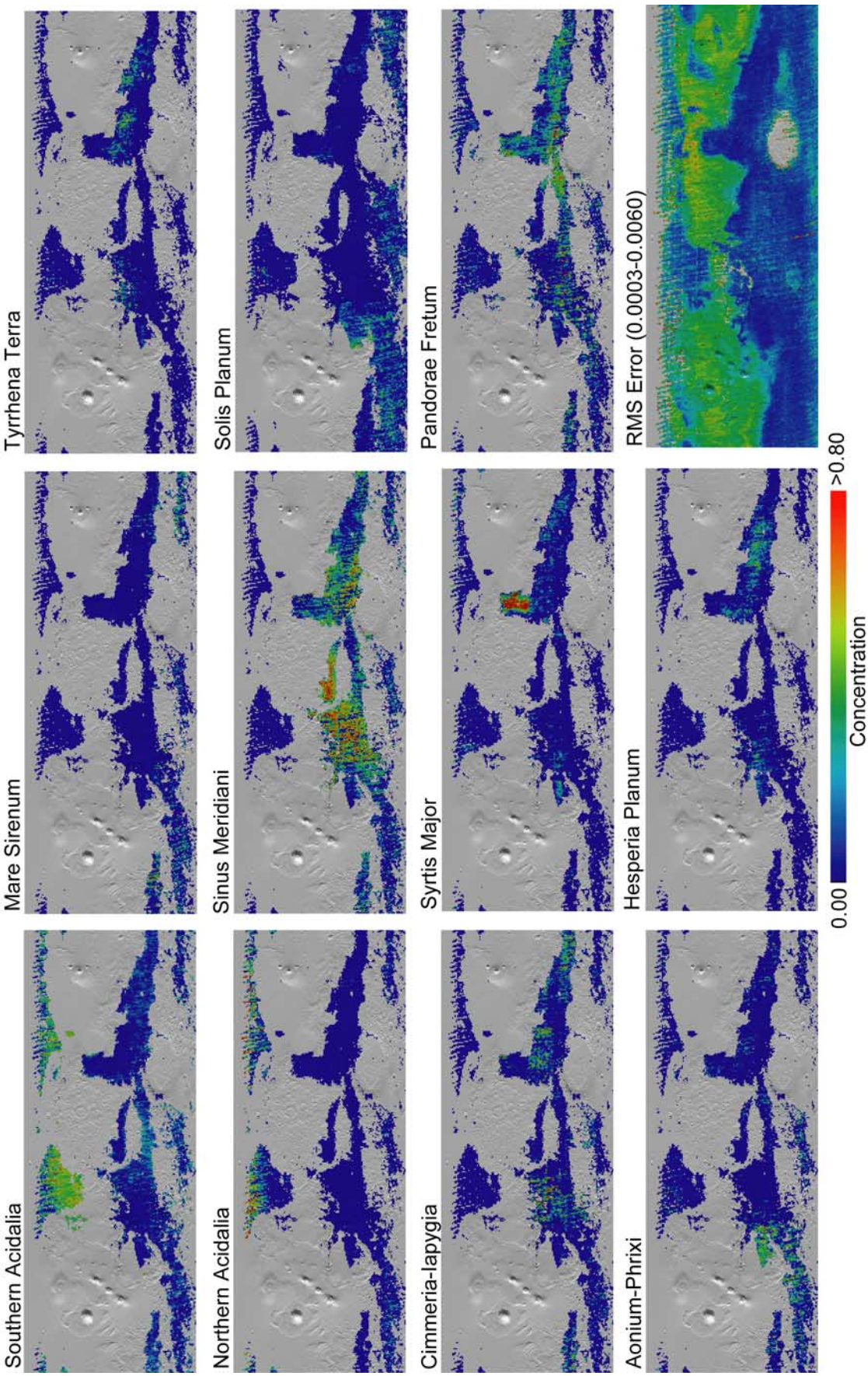

Figure 13. Representative surface spectral end-member concentration maps (one pixel-per-degree). Surfaces with clear-period TES albedo values >0.15 are masked out (except Solis, where albedo values >0.17 are masked out). The area shown for each map is 360° of longitude centered on 0°, and latitudes between 70°S to 70°N. The background image for each map is MOLA shaded relief.

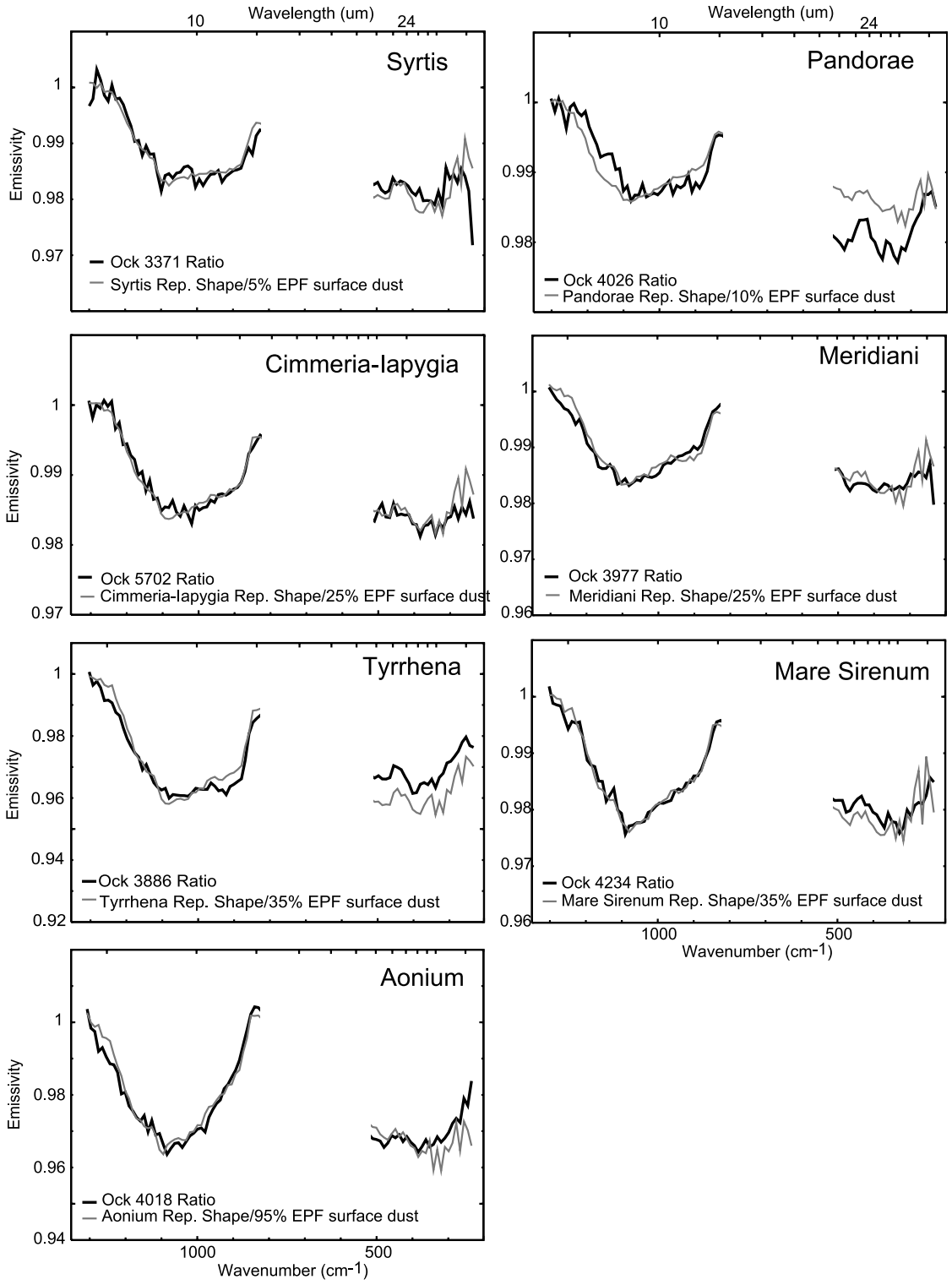

Figure 14. Spectral ratios from regions that were mapped with high concentrations of the Syrtis, Pandorae, Protei, Mare Sirenum, Tyrrhena, Meridiani, and Aonium-Phrixi representative shapes. Each ratio is compared with the representative shape divided by a fraction of the EPF surface dust end-member (section 4.6). Effective emissivity ratios and surface emissivity ratios are normalized to the same spectral contrast for each plot. The worst spectral match between effective emissivity ratio and surface emissivity-EPF surface dust ratio is Pandorae. Tyrrhena and Meridiani show some mismatch at longer wavelengths however the overall trends in that wavelength region exhibited by the effective emissivity ratio are similar to the respective representative surface shape.

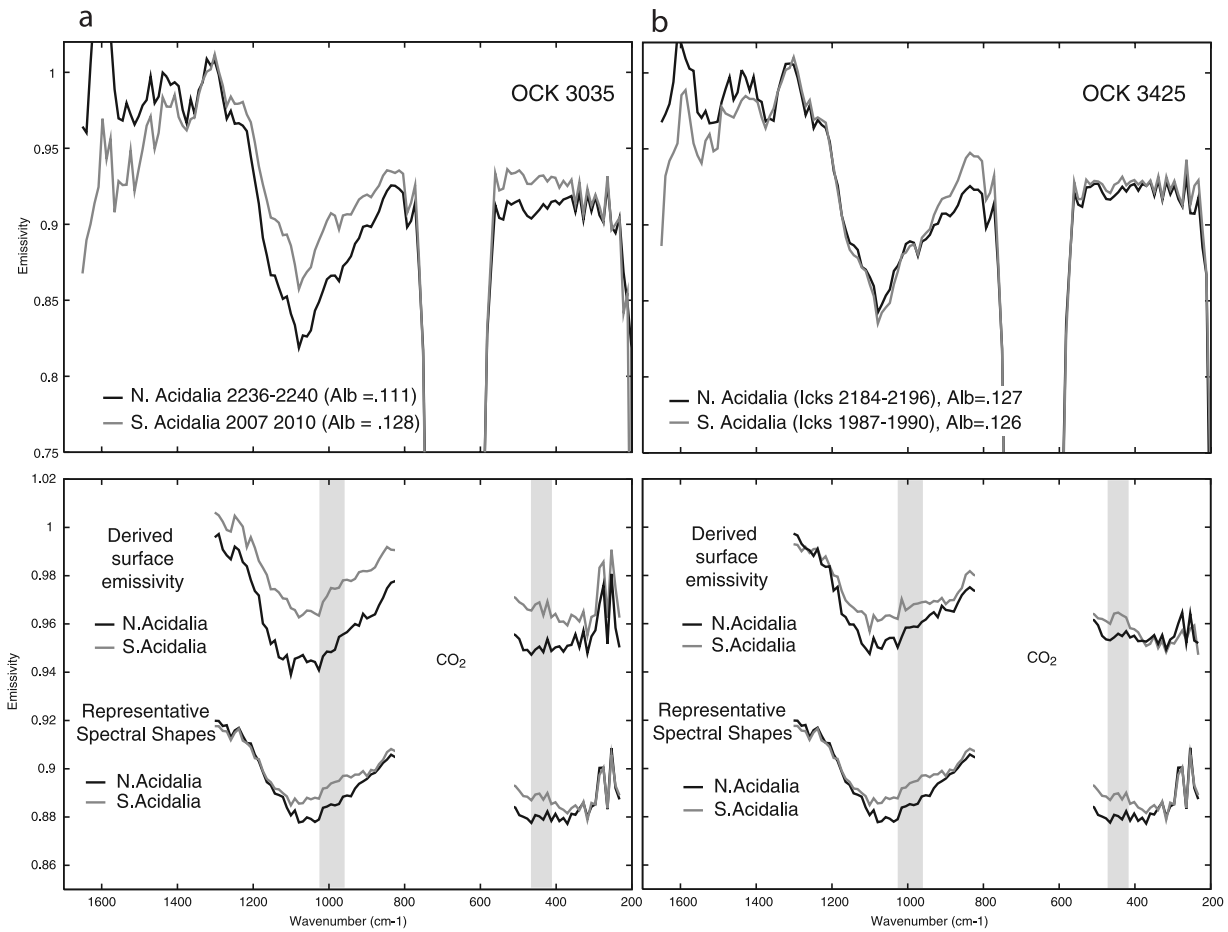

Figure 15. Spectra from orbits that transition southern and northern Acidalia. (a) OCK 3035, comparison of northern and southern Acidalia. (b) OCK 3425, comparison of northern and southern Acidalia. For both Figures 15a and 1b, the top plot shows non–atmospherically corrected effective emissivity spectra. Some of the difference at low wave numbers is due to water vapor, but some is due to surface variation. The bottom plot shows derived surface emissivity from the spectra in the top plot and the representative regional spectra for comparison. Major differences at ~975 and ~450 cm^{-1} are observed, consistent with the derived representative shapes for northern and southern Acidalia.

high concentrations of the Hesperia, Solis Planum, northern and southern Acidalia representative shapes did not exhibit the conditions necessary for ratioing, however the atmospheric variability and wide orbit range used to derive the shape suggest that the derived surface emissivity is reliable. For southern Acidalia and northern Acidalia, we show two orbits that traverse these regions (section 4.6) (Figure 15). Spectral differences between these two regions are present from 300–500 cm^{-1}, indicating real surface variability is present.

[56] Tyrrhena shows some mismatch between the spectral ratio and representative surface shape, however the long-wavelength portions are similar. Although the spectral match is poorer than the other shapes, its distinct distribution and the atmospheric variability within the data set used to derive the Tyrrhena shape (Figure 12) suggest it should not be discarded. In addition, it cannot be ruled out that mismatch between ~850 and 1000 cm^{-1} is due to local variability within the region where the ratio was derived. One region, Pandorae, failed to meet either of our corroborative criteria in terms of an adequate spectral match to the ratio spectrum and atmospheric variability in the spectra used to derive the shape (Figures 12 and 14). Exclusion of this shape from the potential end-member set when producing the concentration maps in section 5.2 has no significant change in the distributions of the other representative shapes. The only notable difference is that the Aonium-Phrixi representative shape is used to model surface emissivity from the Pandorae region.

5.4. Comparison With Surface Type 1 and 2 Spectral Shapes and Distributions

[57] The representative low-albedo region spectra are similar in shape to the originally derived Surface Types 1 and 2, and the intermediate surface type [*Bandfield et al.*, 2000b]; all shapes have major absorptions between 825–1301 cm^{-1} and 225–500 cm^{-1}, consistent with silicate materials. If the representative spectral shapes that are most similar to the Surface Type 1 end-member are averaged, a reasonable match to the Type 1 end-member of *Bandfield et al.* [2000b] is produced, and likewise for Surface Type 2, indicating that the original surface types [*Bandfield et al.*,

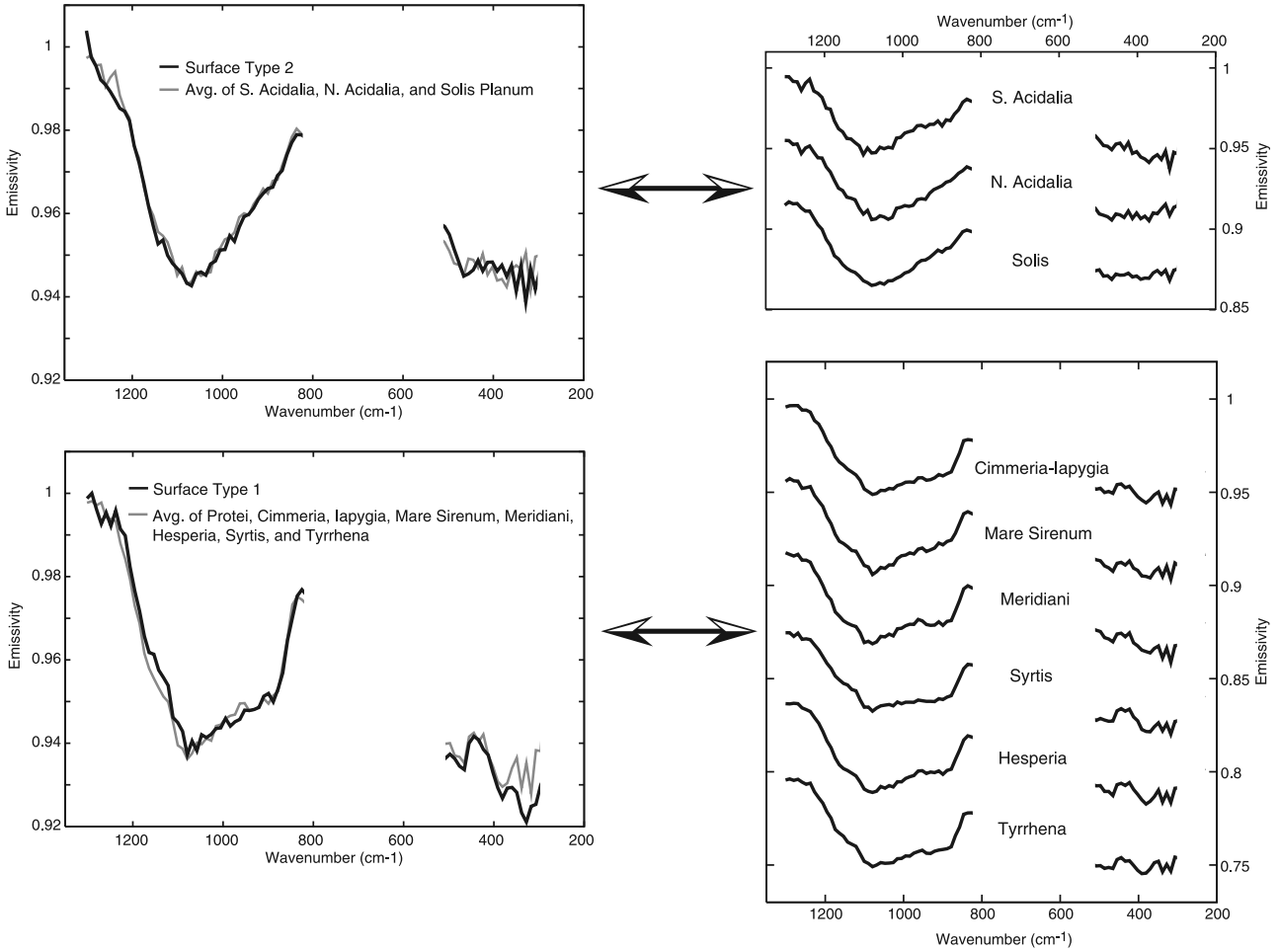

Figure 16. Average of N. Acidalia, S. Acidalia and Solis Planum representative regional shapes compared with the Surface Type 2 end-member of *Bandfield et al.* [2000b], and average of Cimmeria-Iapygia, Mare Sirenum, Meridiani, Hesperia, Syrtis and Tyrrhena representative regional shapes compared with the Surface Type 1 end-member of *Bandfield et al.* [2000b]. Both spectra compare well with the two original end-members, reinforcing the conclusion that the Surface Type 1 and Type 2 spectral shapes are descriptive of the average of all low-albedo regions [*Bandfield et al.*, 2000b].

2000b] are truly representative of the *average* of all low-albedo regions (Figure 16).

[58] If the regions identified here are mixtures of these two end-members, then it should be possible to fit the regional spectra using only Surface Types 1 and 2. Figure 17 shows the best model fits to the representative shapes of this work using only Surface Types 1 and 2. Although features are broadly well-modeled using only these end-members, there are visible departures between the model and measured spectra, indicating that other surface components are present. This suggests that some areas that were previously mapped as mixtures of Surface Types 1 and 2 may be better represented as a different surface type, rather than a mixture of the two end-members.

[59] Using the regionally derived spectral shapes from this work in place of Surface Types 1 and 2 to model global surface emissivity gives lower RMS errors than that of *Bandfield et al.* [2000b] for low-albedo regions. Lower RMS errors are to be expected when a larger potential end-member set is used, however. From comparison of the original RMS error and Surface Type concentration maps of *Bandfield et al.* [2000b] with the maps of this work, it is clear that some areas are better modeled with one or more of the regionally derived shapes than with a mixture of only Surface Types 1 and 2 (or the intermediate surface type). The benefit of using these additional spectra is that small surface spectral features are better represented. Areas that were previously mapped as partially consisting of a Surface Type 2 component no longer require a Surface Type 2-like spectral shape to best model the surface spectrum. Although these areas may contain some of the spectral features/compositional phases found in the Surface Type 2 end-member, this refinement allows for easier interpretation of the distributions of spectral shapes defined in this and previous work.

6. Discussion

6.1. Causes of Spectral Shape Differences

[60] There are several effects that could contribute to the observed differences in spectral shape. Regional differences in bulk mineralogy could cause the observed variations. The

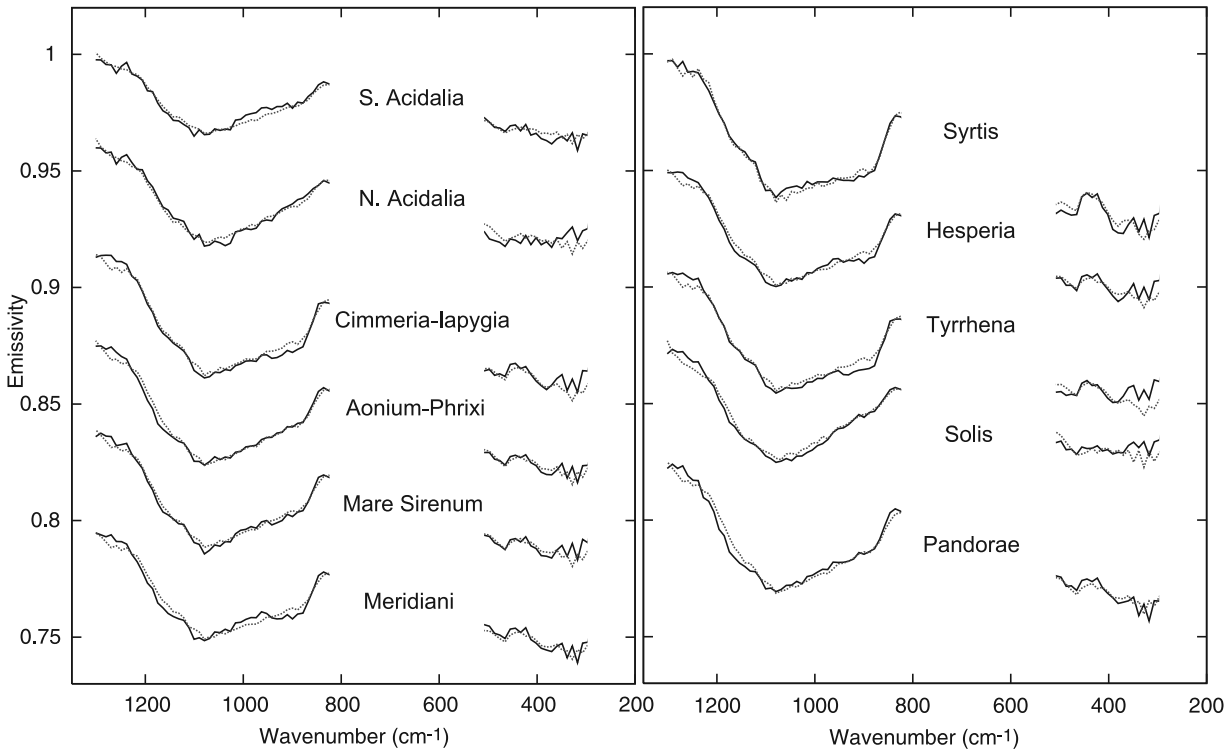

Figure 17. Best model fits (dotted lines) of the eleven representative low-albedo region shapes (solid lines) using Surface Types 1 and 2 [*Bandfield et al.*, 2000b]. Some shapes are well-modeled using only these end-members; others have spectral features that are not fit as well, suggesting other phases are present.

potential control of bulk mineralogy on the observed spectral differences and the implications are discussed in a companion paper (Paper 2). Other effects that could influence the thermal emission spectrum of a surface are mixtures of bulk mineralogy with precipitated coatings, weathering rinds, and/or loose surface dust. Controlled deposition of amorphous silica coatings on basalts in a laboratory [*Kraft et al.*, 2003] as well as natural coatings on rocks [*Minitti et al.*, 2003, 2005] have been shown to significantly alter the thermal emission spectrum compared to a fresh cut surface. Opaline coatings only 3–7 μm thick may completely mask the spectral character of the substrate [*Kraft et al.*, 2003; *Minitti et al.*, 2003], and even coatings as thin as $\sim$0.5 μm still have a significant spectral contribution to the measured spectrum, indicating nonlinear spectral mixing of pure amorphous silica with the substrate [*Kraft et al.*, 2003]. Natural weathering rinds can have a similar effect [*Kraft et al.*, 2005; *Michalski et al.*, 2005a]. Finally, loose palagonitic dust coatings as thin as 10–15 μm [*Graff*, 2003] or $\sim$50 μm [*Johnson et al.*, 2002b] on basaltic rocks produce changes in the thermal emission spectrum comparable to the spectral differences mapped in this work.

[61] One thing that must be considered is the physical nature of low-albedo surfaces that are measured with TES. For a surface to maintain a low albedo, it is likely to have a significant sand component that is able to saltate and clean itself of dust [e.g., *Thomas et al.*, 1984; *Christensen*, 1988]. This is consistent with low-albedo region particle sizes derived from Viking and TES thermal inertia data [e.g., *Kieffer et al.*, 1977; *Edgett and Christensen*, 1991; *Presley and Christensen*, 1997; *Mellon et al.*, 2000]. Although most low-albedo regions have a significant rock component [*Christensen*, 1986; *Nowicki and Christensen*, 1999], there are almost no areas on Mars where, at the footprint of a TES pixel, rocks are the dominant component. In addition, because rocks are colder than sands during the day, their contribution to the measured radiance is lower. The question of whether coatings and/or rinds are present on sand grains becomes important when discussing their contribution to TES surface emissivity spectra of low-albedo regions, especially in areas of low rock abundance. In addition, the question of whether coatings and/or rinds survive on rocks that are surrounded by saltating sand grains must also be considered. Although amorphous silica coatings are less susceptible to abrasion than calcrete and rock varnish coatings [*Kraft and Greeley*, 2000], desert silica "glazes" found on Earth are weak and removed easily in an eolian environment [*Dorn*, 1998]. However, there have been reports of possible amorphous silica coatings on dune sands in western Egypt [*El-Baz and Prestel*, 1980]. If coatings are present, they likely formed recently enough to not have been removed by saltation.

[62] On Mars, apparently resilient coatings are present on rocks at the MER Spirit Rover landing site in Gusev Crater [e.g., *Squyres et al.*, 2004], and probably at the Viking [e.g., *Arvidson et al.*, 1989; *Guinness et al.*, 1997] and Pathfinder [*Johnson et al.*, 1999; *McSween et al.*, 1999] landing sites. However, the average TES albedo of those landing sites and surrounding areas range from $\sim$0.22 to 0.30 [*Golombek et al.*, 2003]. Those sites are not representative of the low-

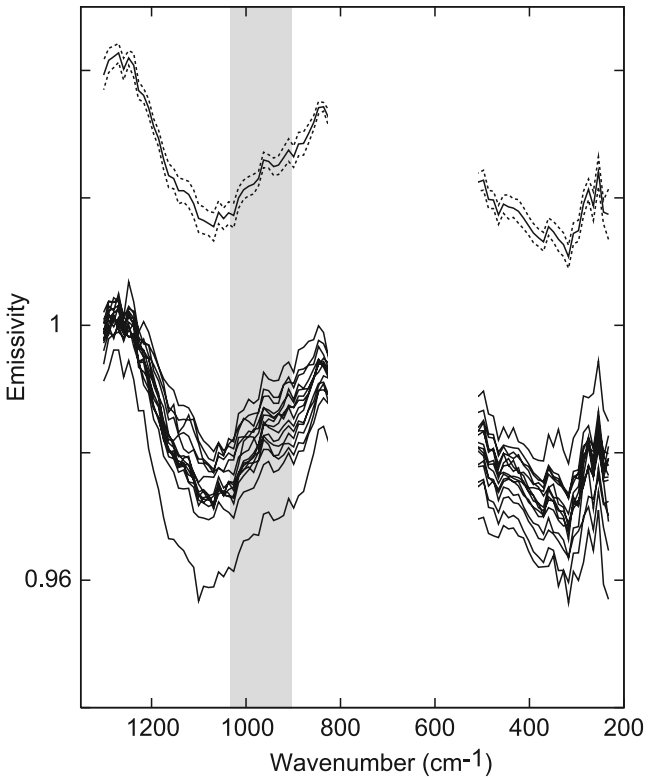

Figure 18a. Fifteen randomly selected surface emissivity spectra from intermediate albedo regions (albedo values ranged from ~0.16–0.19). Spectra are selected from the 1 pixel-per-degree surface emissivity cube derived by *Bandfield* [2002]. The top set of spectra are the average and $\pm 1\sigma$ from the lower set of spectra.

albedo regions of this study. At the Opportunity Rover landing site in Meridiani Planum, few rocks are present, with the exception of the extensive sulfate-rich outcrop, which is also probably not representative of the majority of rocks of the low-albedo regions in this study. Instead, basaltic sands and hematite-rich granules dominate the surface. Future studies focused on the survivability of rinds/coatings on sand grains and on rocks in active saltating environments (similar to that of *Kraft and Greeley* [2000]) will shed light on the contribution of those materials to TES emissivity spectra.

[63] The albedo constraint in this work precludes significant influences from loose dust coatings; however one exception in this work may be southern Acidalia. The southern Acidalia shape has a slightly lower spectral contrast and is mostly concentrated in the highest-albedo areas (~0.13–0.15) examined in this study. The spectral contrast and higher associated albedo suggests either a slightly finer particle size than surrounding dark regions or a greater abundance of surface dust that is mixed with rocks and sand. The thermal inertia values for southern Acidalia (~225–340 J m^{-2} K^{-1} $s^{-1/2}$ [*Mellon et al.*, 2000]) are 20–140 J m^{-2} K^{-1} $s^{-1/2}$ higher than Syrtis Major, which is the darkest region on Mars, suggesting that a thin or discontinuous layer of surface dust mixed with rocks and sand is more likely. This suggestion is supported by the observation that the southern Acidalia spectral shape is used in combination with EPF surface dust to model the emissivity of higher-albedo regions (section 5.2). Finally, we note a broad, weakly concave-downward spectral feature between 900 and 1020 cm^{-1} that is present in the southern Acidalia shape (derived in this work, Figure 11, and by *Moersch et al.* [1997]). This feature, also characterized by a steep rise in emissivity at ~1020 cm^{-1}, is commonly observed in intermediate-albedo (~0.16–0.19) regions (Figures 18a and 18b). In addition, a similar spectral feature has been observed in laboratory thermal emission spectra of basalts and andesites with ~11–15 μm palagonitic dust coatings (Figure 19) [*Graff*, 2003]. Although these observations suggest the possibility, this feature may not necessarily equate with the presence of thin dust coatings, as it is also apparent in a few of the lower-albedo representative spectral shapes of this work (Figure 11). However, at least in the case of southern Acidalia, the representative spectrum is similar to some intermediate albedo surfaces not only in the spectral region discussed above, but across the full wavelength range (Figure 18b). This further supports the idea that the southern Acidalia emissivity is influenced by thin (<15 μm) dust coatings.

[64] In summary, dust coatings could be partially contributing to the measured spectra in some areas, but it is more likely that variations in surface mineralogy exhibit the strongest control on observed spectral variations in low-albedo regions. The presence/absence of rinds and mineral coatings is less clear. Use of geologic context, other data sets such as from the Gamma Ray Spectrometer (GRS), the Mars Express Observatoire pour la Mineralogie, l'Eau, les Glaces, et l'Activite (OMEGA) [*Bibring et al.*, 2005] and the Mars Reconnaissance Orbiter Compact Reconnaissance Imaging Spectrometer for Mars (CRISM), and future rover mission data may help to clarify the presence and likely contribution of rinds and mineral coatings to IR spectra of low-albedo regions.

6.2. Spectral Variation Between Martian Dark Regions

[65] Surface Types 1, 2 and the intermediate type [*Bandfield et al.*, 2000b] accurately describe the average of Martian dark regions and provide useful reference spectra for spectral studies (section 5.4, Figure 14). However, it is important to emphasize that many low-albedo surfaces that

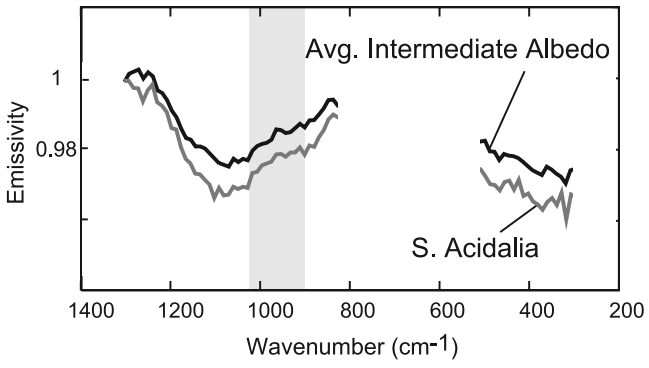

Figure 18b. Comparison of the average intermediate albedo spectral shape from Figure 18a and the Southern Acidalia representative surface emissivity shape from Figure 11. The shaded area indicates the wavelength range of the concave-downward spectral feature discussed in the text.

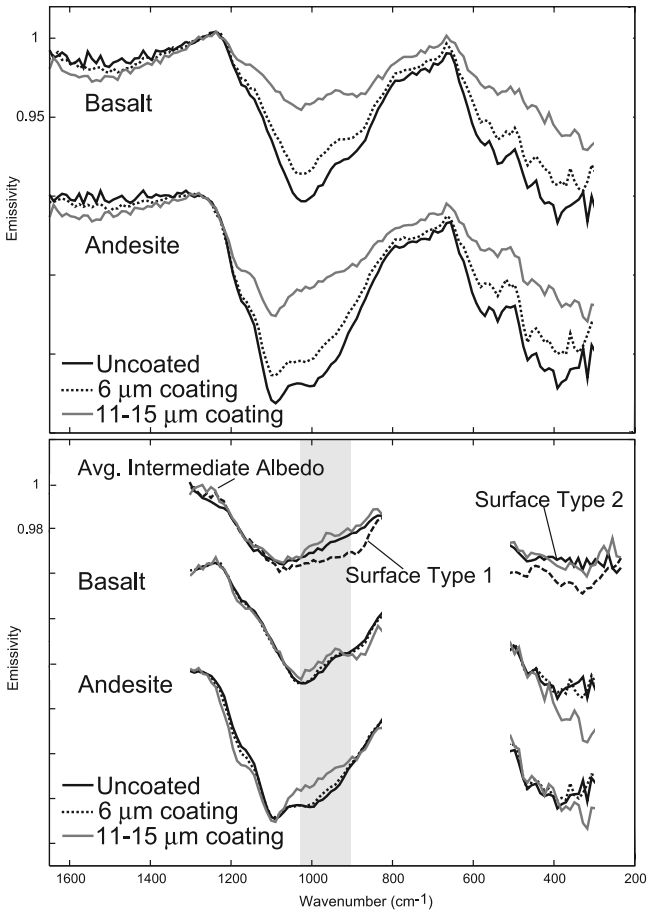

Figure 19. Laboratory spectra of dust-coated basalts compared with intermediate albedo region spectra. (a) Laboratory thermal emission spectra of basalt and andesite substrates with 6 and 11–15 μm palagonitic dust coatings [*Graff*, 2003]. Basaltic and andesitic series are offset by 0.10 emissivity. (b) Spectra from Figure 19a, normalized to the same spectral contrast and compared with the average intermediate albedo spectral shape from Figure 18a, and Surface Types 1 and 2 [*Bandfield et al.*, 2000b] (also normalized to the same spectral contrast). The shaded area indicates the wavelength range of the concave-downward spectral feature discussed in the text. Spectra are offset for clarity.

were originally mapped as one or a mixture of the two global end-members have subtle but mappable differences in spectral response from those end-members. These differences could reflect small variations in primary or secondary mineralogy, which in turn could indicate differences in alteration or volcanic history. A spectral difference between southern and northern Acidalia Planitia may be due in part to a small amount of dust cover in southern Acidalia. However, long-wavelength features are also different between these two regions (Figure 11), suggesting that additional compositional differences are present, consistent with previous studies of Acidalia [*Farrand et al.*, 2000; *Noe Dobrea et al.*, 2003; *Wyatt et al.*, 2003].

[66] Global spectral variations beyond only three surface types are consistent with previous TES, ISM, HST, OMEGA, GRS and THEMIS mineral mapping results, which show variations in relative mineral and elemental abundances across the surface [e.g., *Mustard and Sunshine*, 1995; *Bell et al.*, 1997; *Mustard et al.*, 1997; *Bandfield*, 2002; *Bibring et al.*, 2005; *Christensen et al.*, 2005; *Rogers et al.*, 2005; *Le Mouélic et al.*, 2006; *Taylor et al.*, 2006]. The key point is that by adding additional surface spectral shapes to an end-member set, the original surface type distributions are refined. This should be considered when using geologic context as a constraint for interpreting derived mineralogy of the two original surface types.

6.3. A Refined "Surface Type 2" Distribution

[67] Much attention has been given to the Surface Type 2 component derived for some Martian low-albedo regions, because it contains one or more amorphous or poorly crystalline high-silica phases that may be interpreted as primary volcanic glass, or a number of secondary coatings and mineraloids. Some studies have focused on either promoting or challenging the possible alternative materials that may substitute for the SiK glass component originally reported for Surface Type 2 [*Bandfield et al.*, 2000b; *Hamilton et al.*, 2001], such as phyllosilicates [*Wyatt and McSween*, 2002; *Hamilton et al.*, 2003a; *Ruff*, 2003; *Koeppen and Hamilton*, 2005; *Michalski et al.*, 2005b], secondary amorphous silica coatings [*Wyatt and McSween*, 2002; *Kraft et al.*, 2003; *Michalski et al.*, 2003], palagonites [*Morris et al.*, 2003] or zeolites [*Ruff*, 2004]. Other studies have attempted to use geologic context/reasoning to deduce the most likely explanation for the high-silica component measured for Surface Type 2 areas [*Ruff and Hamilton*, 2001; *Wyatt and McSween*, 2002; *McLennan*, 2003; *Wyatt et al.*, 2003, 2004; *Michalski et al.*, 2005b; *Christensen et al.*, 2005].

[68] The concentration maps from this work indicate that surfaces with the highest concentrations of high-silica phases and "Surface Type 2"-like spectral character are mostly confined to the northernmost part of the lowland plains, and Solis Planum (the Northern Acidalia and Solis Planum distributions, Figure 13). Although surfaces with some of the characteristic Surface Type 2 mineralogical components are likely present elsewhere, this has important implications for the interpretation of the geologic context of pure Surface Type 2. First, the Surface Type 2 distribution is not as widespread in the highlands, or the northern plains, as previously suggested. Areas with high spectral contrast that are the closest spectral match to the original Surface Type 2 spectral shape, besides northern Acidalia and Solis Planum [*Bandfield*, 2002], are the north polar dunes [*Bandfield et al.*, 2002], a small bedrock outcrop in the Nili Patera caldera of Syrtis Major [*Ruff and Hamilton*, 2001; *Christensen et al.*, 2005], and a few isolated locations in the southern mid to high latitudes [*Bandfield*, 2002; *Aben*, 2003] (also this work, Figure 13). The fact that the largest distribution of the pure Surface Type 2-like spectrum (Northern Acidalia representative shape, section 5.2) is located in northern Acidalia, which is mapped as a basin in which sediments may have been transported and reworked by glacial or fluvial processes [e.g., *Tanaka et al.*, 2003], supports the idea that the high-silica phase in the spectrum represents a coating or weathering rind [*Michalski et al.*, 2005b]. Also, aside from the high concentrations in Solis Planum, the

major occurrences of Surface Type 2-like spectra are primarily found in mid- to high-latitude regions, also supporting an alteration product interpretation for the high-silica phase(s) [*Wyatt et al.*, 2004; *Michalski et al.*, 2005b]. However, there are clearly areas on Mars where volcanic glass is the most viable phase, such as Nili Patera [*Christensen et al.*, 2005], and also areas where coatings are less likely to persist, such as the north polar dunes [*Bandfield et al.*, 2002]. This suggests that multiple mechanisms are needed to explain the global distribution of high-silica phase(s). Finally, although an alteration interpretation for Surface Type 2 areas in the northern plains and mid- to high-latitude regions is more likely, volcanic glass cannot be completely eliminated as the explanation for the high-silica phase(s) in Surface Type 2.

6.4. Comments on the Southern Mid- to High-Latitude Regions

[69] This work focused on large dark regions that exhibit TES albedo values less than 0.15 (except for Solis Planum) and high spectral contrast. These constraints exclude a large portion of the southern hemisphere surfaces between ~30°S and 70°S from examination (Figure 13). Several small dark regions are scattered throughout this latitude range, however, and detailed examination of some of these regions suggest that some areas are similar to Type 2 [*Bandfield*, 2002] and other areas are similar to Type 1 [*Aben*, 2003; *Fenton et al.*, 2003].

[70] Previous authors suggested a correlation of increased Surface Type 2 abundance [*Wyatt et al.*, 2004] and increased plagioclase and high-silica components abundance, decreased pyroxene and olivine abundance [*Michalski et al.*, 2005b] with increasing latitude, citing previously derived mineral and surface type concentration maps [*Bandfield et al.*, 2000b; *Bandfield*, 2002]. The proposed correlation with latitude was used to suggest that the high-silica component(s) observed with TES data are more likely to be alteration phases [*Wyatt et al.*, 2004; *Michalski et al.*, 2005b].

[71] Although some portions of the southern mid- to high-latitude regions are low albedo (<0.15) and similar in spectral character and derived mineralogy to northern Acidalia (Figure 13) [*Bandfield*, 2002; *Aben*, 2003; *Rogers and Christensen*, 2007], the Surface Type 2/high-silica phase(s) are not as widely distributed in the southern mid to high latitudes as previously suggested [*Wyatt et al.*, 2004; *Michalski et al.*, 2005b]. Both of those studies did not consider that much of the southern high latitudes have an intermediate to high albedo (two thirds of surfaces exhibit albedo values >0.15) [*Christensen et al.*, 2001], and probably should have been excluded from interpretation, or at least, should not be compared with dark regions in the northern mid to high latitudes, such as Acidalia. As discussed in section 6.1, surface emissivity from some regions with surface albedo values as low as 0.15 may be affected by the influence of loose dust coatings. Additionally, it is not clear that derived emissivity from lower spectral contrast surfaces, even such as those found in intermediate albedo (~0.15–0.19) regions, is reliable (Figure 5, section 3.3). Concentrations of Surface Type 2 [*Bandfield et al.*, 2000b; *Wyatt and McSween*, 2002; *Wyatt et al.*, 2004] and sheet-silicate/glass [*Bandfield*, 2002; *Michalski et al.*, 2005b] in southern high latitudes commonly appear correlated with individual orbit tracks and have poor spatial coherence. The systematic use of these phases to model surface emissivity from the highest-albedo regions (section 3.3), where coarse particulates of these compositions do not exist, further lowers confidence in the derived abundance of these phases in some intermediate albedo (~0.15–0.19) regions. Finally, to date there have been no reports of concentrated phyllosilicates in these regions from OMEGA data [e.g., *Poulet et al.*, 2005].

[72] In summary, the relative lack of mafic minerals observed in large portions of the southern mid- to high-latitude regions [*Michalski et al.*, 2005b] may be due to lower spectral contrast, and possibly increased dust cover, rather than increased weathering of coarse particulate igneous materials. The evidence for snowpack [*Christensen*, 2003], ground ice [*Boynton et al.*, 2002; *Feldman et al.*, 2002] and extensive volatile-rich surfaces in the southern high latitudes [*Malin and Edgett*, 2001; *Mustard et al.*, 2001; *Milliken et al.*, 2003] suggests that secondary phases should become more abundant, and mafic minerals less abundant, in these areas [*Wyatt et al.*, 2004; *Michalski et al.*, 2005b]. However, it is not clear that the presence of those phases in lower spectral contrast regions can be detected and quantified with TES data using only the linear deconvolution technique. Supporting surface-atmosphere separation techniques could be used to gain confidence in the accuracy of linear deconvolution-derived surface emissivity in the lower spectral contrast regions.

7. Conclusions

[73] 1. There are several methods for surface-atmosphere separation, surface analysis and spatial visualization of composition that have been developed for TES data. When surface emissivity and mineralogy are the desired quantities to be determined, all of these methods should be considered, depending on the nature of the study (example: global versus local) and the nature of the surface of interest (example: coarse particulate, cemented, or dusty). The use of two or more methods, where possible, increases confidence in the derived surface emissivity.

[74] 2. Deconvolution of TES spectra with excessive levels of atmospheric water ice and dust (including levels below constraints used in some of the previous TES studies) can introduce false spectral features into the derived surface emissivity spectrum. Similarly, linear deconvolution of spectra from high-albedo surfaces (≥0.20) does not always properly remove atmospheric and surface components, even if a surface dust spectrum [*Bandfield and Smith*, 2003] is included, resulting in incorrect derived surface emissivity. The phases that are most commonly used to deconvolve these surfaces are high-silica phase(s) and feldspars.

[75] 3. Although not conclusive, results from this and previous work suggest that the surface emissivity from some intermediate-albedo surfaces (~0.15–0.19) may be influenced by thin coatings of dust that do not combine linearly with the substrate.

[76] 4. Eleven spectral shapes were found to be representative of the 29 low-albedo regions studied. The differences between these spectral shapes are subtle, however their

distributions are spatially contiguous, which builds confidence that they are due to real surface variations. Regional-scale spectral variations are present within areas previously mapped as Surface Type 1 or a mixture of the two surface types, suggesting variations in mineral abundance among basaltic units. For example, Syrtis Major, which was the Surface Type 1 type locality, is distinct from the terrains that were also previously mapped as Type 1.

[77] 5. An average of shapes that are similar to Surface Type 1 produces an excellent match to Type 1 [*Bandfield et al.*, 2000b], and likewise for Surface Type 2, indicating that the original end-members are accurately representative of the average of all low-albedo regions.

[78] 6. Modeling global surface emissivity with the representative shapes of this work refines the distribution of Surface Types 1 and 2. Type 2-like surfaces (corresponding to the N. Acidalia and Solis Planum representative shapes of this work) are less extensive than previously thought, and are mostly confined to the northern lowlands. Additional high concentrations are found in the southern high latitudes and in Solis Planum, consistent with previous studies [*Bandfield*, 2002; *Aben*, 2003; *Wyatt et al.*, 2004; *Michalski et al.*, 2005b]. The global distributions indicate that the origin of Surface Type 2 cannot be adequately explained by a single process.

[79] 7. The differences between most of the representative surface shapes are likely due to small variations in surface mineralogy. A companion paper (Paper 2) discusses the mineralogy and geologic context associated with each spectral shape, and addresses the relative contribution of primary and secondary mineralogy to the spectral variations discussed in this work.

[80] **Acknowledgments.** The authors thank Vicky Hamilton for providing the olivine and pigeonite spectra used in this work, Steve Ruff for the zeolite spectra, and Mike Kraft for the Al-opal spectrum. We also thank Tim Glotch for an early review of this manuscript, and Robin Fergason for contributing useful discussions. We sincerely appreciate the formal reviews from Scott Anderson and Bill Farrand, which helped to clarify this paper. The Mars Global Surveyor Project Office provided support for this work.

References

Aben, L. K. (2003), Compositional and thermophysical analysis of Martian aeolian dunes, M. S. thesis, Ariz. State Univ., Tempe.

Adams, J. B. (1968), Lunar and Martian surfaces—Petrologic significance of absorption bands in near-infrared, *Science*, *159*(3822), 1453–1455.

Arvidson, R. E., J. L. Gooding, and H. J. Moore (1989), The Martian surface as imaged, sampled, and analyzed by the Viking landers, *Rev. Geophys.*, *27*(1), 39–60.

Bandfield, J. L. (2002), Global mineral distributions on Mars, *J. Geophys. Res.*, *107*(E6), 5042, doi:10.1029/2001JE001510.

Bandfield, J. L. (2003), Martian global surface mineralogy from the Thermal Emission Spectrometer: Surface emissivity, mineral map, and spectral end-member data products, paper presented at Sixth International Conference on Mars, Lunar and Planet. Inst., Houston, Tex.

Bandfield, J. L., and M. D. Smith (2003), Multiple emission angle surface-atmosphere separations of Thermal Emission Spectrometer data, *Icarus*, *161*, 47–65.

Bandfield, J. L., P. R. Christensen, and M. D. Smith (2000a), Spectral data set factor analysis and end-member recovery: Application to analysis of Martian atmospheric particulates, *J. Geophys. Res.*, *105*(E4), 9573–9587.

Bandfield, J. L., V. E. Hamilton, and P. R. Christensen (2000b), A global view of Martian surface compositions from MGS-TES, *Science*, *287*(5458), 1626–1630.

Bandfield, J. L., K. S. Edgett, and P. R. Christensen (2002), Spectroscopic study of the Moses Lake dune field, Washington: Determination of compositional distributions and source lithologies, *J. Geophys. Res.*, *107*(E11), 5092, doi:10.1029/2000JE001469.

Bandfield, J. L., T. D. Glotch, and P. R. Christensen (2003), Spectroscopic identification of carbonate minerals in the Martian dust, *Science*, *301*(5636), 1084–1087.

Bandfield, J. L., V. E. Hamilton, P. R. Christensen, and H. Y. McSween Jr. (2004), Identification of quartzofeldspathic materials on Mars, *J. Geophys. Res.*, *109*, E10009, doi:10.1029/2004JE002290.

Bell, J. F., M. J. Wolff, P. B. James, R. T. Clancy, S. W. Lee, and L. J. Martin (1997), Mars surface mineralogy from Hubble Space Telescope imaging during 1994–1995: Observations, calibration, and initial results, *J. Geophys. Res.*, *102*(E4), 9109–9123.

Bibring, J. P., et al. (2005), Mars surface diversity as revealed by the OMEGA/Mars Express observations, *Science*, *307*(5715), 1576–1581.

Boynton, W. V., et al. (2002), Distribution of hydrogen in the near surface of Mars: Evidence for subsurface ice deposits, *Science*, *297*(5578), 81–85.

Christensen, P. R. (1986), The spatial distribution of rocks on Mars, *Icarus*, *68*, 217–238, 1986.

Christensen, P. R. (1988), Global albedo variations on Mars—Implications for active aeolian transport, deposition, and erosion, *J. Geophys. Res.*, *93*(B7), 7611–7624.

Christensen, P. R. (1998), Variations in Martian surface composition and cloud occurrence determined from thermal infrared spectroscopy: Analysis of Viking and Mariner 9 data, *J. Geophys. Res.*, *103*(E1), 1733–1746.

Christensen, P. R. (2003), Formation of recent Martian gullies through melting of extensive water-rich snow deposits, *Nature*, *422*(6927), 45–48, 2003.

Christensen, P. R., et al. (1992), Thermal Emission Spectrometer Experiment: Mars Observer Mission, *J. Geophys. Res.*, *97*(E5), 7719–7734.

Christensen, P. R., J. L. Bandfield, M. D. Smith, V. E. Hamilton, and R. N. Clark (2000a), Identification of a basaltic component on the Martian surface from Thermal Emission Spectrometer data, *J. Geophys. Res.*, *105*(E4), 9609–9621.

Christensen, P. R., J. L. Bandfield, V. E. Hamilton, D. A. Howard, M. D. Lane, J. L. Piatek, S. W. Ruff, and W. L. Stefanov (2000b), A thermal emission spectral library of rock-forming minerals, *J. Geophys. Res.*, *105*(E4), 9735–9739.

Christensen, P. R., et al. (2000c), Detection of crystalline hematite mineralization on Mars by the Thermal Emission Spectrometer: Evidence for near-surface water, *J. Geophys. Res.*, *105*(E4), 9623–9642.

Christensen, P. R., et al. (2001), Mars Global Surveyor Thermal Emission Spectrometer experiment: Investigation description and surface science results, *J. Geophys. Res.*, *106*(E10), 23,823–23,871.

Christensen, P. R., et al. (2003), Morphology and composition of the surface of Mars: Mars Odyssey THEMIS results, *Science*, *300*(5628), 2056–2061.

Christensen, P. R., et al. (2004a), Initial results from the Mini-TES experiment in Gusev crater from the Spirit rover, *Science*, *305*(5685), 837–842.

Christensen, P. R., et al. (2004b), Mineralogy at Meridiani Planum from the Mini-TES experiment on the Opportunity Rover, *Science*, *306*(5702), 1733–1739.

Christensen, P. R., et al. (2005), Evidence for magmatic evolution and diversity on Mars from infrared observations, *Nature*, *436*(7052), 882.

Dorn, R. I. (1998), *Rock Coatings*, 429 pp., Elsevier, New York.

Edgett, K. S., and P. R. Christensen (1991), The particle size of Martian aeolian dunes, *J. Geophys. Res.*, *96*(E5), 22,765–22,776.

El-Baz, F., and D. Prestel (1980), Desert varnish on sand grains from the western Desert of Egypt: Importance of the clay component and implications to Mars, *Lunar Planet. Sci.*, *XI*, 254–256.

Erard, S., J.-P. Bibring, and Y. Langevin (1990), Determination of spectral units in the Syrtis Major-Isidis Planitia region from Phobos/ISM observations, *Lunar Planet. Sci.*, *XX*, 327.

Farrand, W. H., J. F. Bell III, R. V. Morris, and M. J. Wolff (2000), Global color units on Mars from 199 9 HST/WFPC2 imaging data, *Bull. Am. Astron. Soc.*, *32*, Abstract 1119.

Feldman, W. C., et al. (2002), Global distribution of neutrons from Mars: Results from Mars Odyssey, *Science*, *297*(5578), 75–78.

Fenton, L. K., J. L. Bandfield, and A. W. Ward (2003), Aeolian processes in Proctor Crater on Mars: Sedimentary history as analyzed from multiple data sets, *J. Geophys. Res.*, *108*(E12), 5129, doi:10.1029/2002JE002015.

Gillespie, A. R. (1992), Spectral mixture analysis of multispectral thermal infrared images, *Remote Sens. Environ.*, *42*(2), 137–145.

Glotch, T. D., and P. R. Christensen (2005), Geologic and mineralogic mapping of Aram Chaos: Evidence for a water-rich history, *J. Geophys. Res.*, *110*, E09006, doi:10.1029/2004JE002389.

Glotch, T. D., R. V. Morris, P. R. Christensen, and T. G. Sharp (2004), Effect of precursor mineralogy on the thermal infrared emission spectra of hematite: Application to Martian hematite mineralization, *J. Geophys. Res.*, *109*, E07003, doi:10.1029/2003JE002224.

Golombek, M. P., et al. (2003), Selection of the Mars Exploration Rover landing sites, *J. Geophys. Res.*, *108*(E12), 8072, doi:10.1029/2003JE002074.

Graff, T. G. (2003), Effects of dust coatings on visible, near-infrared, thermal emission and Mossbauer spectra: Implications for mineralogical remote sensing of Mars, M. S. thesis, Ariz. State Univ., Tempe.

Guinness, E. A., R. E. Arvidson, I. H. D. Clark, and M. K. Shepard (1997), Optical scattering properties of terrestrial varnished basalts compared with rocks and soils at the Viking Lander sites, *J. Geophys. Res.*, *102*(E12), 28,687–28,703.

Hamilton, V. E. (2000), Thermal infrared spectroscopy of the pyroxene mineral series, *J. Geophys. Res.*, *105*(E4), 9701–9716.

Hamilton, V. E., and P. R. Christensen (2005), Evidence for extensive, olivine-rich bedrock on Mars, *Geology*, *33*(6), 433–436.

Hamilton, V. E., and R. D. Schneider (2005), Alteration phases associated with high concentrations of orthopyroxene and olivine on Mars, *Lunar Planet. Sci.*, *XXXVI*, Abstract 2212.

Hamilton, V. E., M. B. Wyatt, H. Y. McSween, and P. R. Christensen (2001), Analysis of terrestrial and Martian volcanic compositions using thermal emission spectroscopy: 2. Application to Martian surface spectra from the Mars Global Surveyor Thermal Emission Spectrometer, *J. Geophys. Res.*, *106*(E7), 14,733–14,746.

Hamilton, V. E., P. R. Christensen, and J. L. Bandfield (2003a), Volcanism or aqueous alteration on Mars?, *Nature*, *421*(6924), 711–712.

Hamilton, V. E., P. R. Christensen, H. Y. McSween, and J. L. Bandfield (2003b), Searching for the source regions of Martian meteorites using MGS TES: Integrating Martian meteorites into the global distribution of igneous materials on Mars, *Meteorit. Planet. Sci.*, *38*(6), 871–885.

Hoefen, T. M., R. N. Clark, J. L. Bandfield, M. D. Smith, J. C. Pearl, and P. R. Christensen (2003), Discovery of olivine in the Nili Fossae region of Mars, *Science*, *302*(5645), 627–630.

Johnson, J. R., et al. (1999), Preliminary results on photometric properties of materials at the Sagan Memorial Station, Mars, *J. Geophys. Res.*, *104*(E4), 8809–8830.

Johnson, J. R., F. Horz, P. G. Lucey, and P. R. Christensen (2002a), Thermal infrared spectroscopy of experimentally shocked anorthosite and pyroxenite: Implications for remote sensing of Mars, *J. Geophys. Res.*, *107*(E10), 5073, doi:10.1029/2001JE001517.

Johnson, J. R., P. R. Christensen, and P. G. Lucey (2002b), Dust coatings on basaltic rocks and implications for thermal infrared spectroscopy of Mars, *J. Geophys. Res.*, *107*(E6), 5035, doi:10.1029/2000JE001405.

Kieffer, H. H., T. Z. Martin, A. B. Peterfreund, B. M. Jakosky, E. D. Miner, and F. D. Palluconi (1977), Thermal and albedo mapping of Mars during the Viking primary mission, *J. Geophys. Res.*, *82*(28), 4249–4291.

Koeppen, W. C., and V. E. Hamilton (2005), Discrimination of glass and phyllosilicate minerals in thermal infrared data, *J. Geophys. Res.*, *110*, E08006, doi:10.1029/2005JE002474.

Kraft, M. D., and R. Greeley (2000), Rock coatings and aeolian abrasion on Mars: Application to the Pathfinder landing site, *J. Geophys. Res.*, *105*(E6), 15,107–15,116.

Kraft, M. D., J. R. Michalski, and T. G. Sharp (2003), Effects of pure silica coatings on thermal emission spectra of basaltic rocks: Considerations for Martian surface mineralogy, *Geophys. Res. Lett.*, *30*(24), 2288, doi:10.1029/2003GL018848.

Kraft, M. D., J. R. Michalski, and T. G. Sharp (2005), Palagonite-like alteration products on the Earth and Mars 2: Secondary mineralogy of crystalline basalts weathered under semi-arid conditions, *Lunar Planet. Sci.*, *XXXVI*, abstract 1376.

Le Mouélic, S., C. Sotin, J.-P. Combe, L. L. A. Gendrin, J. Mustard, J.-P. Bibring, Y. Langevin, B. Gondet, and P. Pinet (2006), Composition of the dust on Mars derived from OMEGA hyperspectral images, *Lunar Planet. Sci.*, *XXXVII*, abstract 1409.

Malin, M. C., and K. S. Edgett (2001), Mars Global Surveyor Mars Orbiter Camera: Interplanetary cruise through primary mission, *J. Geophys. Res.*, *106*(E10), 23,429–23,570.

McCord, T. B. (1969), Comparison of reflectivity and color of bright and dark regions on surface of Mars, *Astrophys. J.*, *156*(1P1), 79–86.

McCord, T. B., and J. A. Westphal (1971), Mars—Narrow-band photometry, from 0.3 to 2.5 microns, of surface regions during 1969 apparition, *Astrophys. J.*, *168*(1), 141–153.

McCord, T. B., R. N. Clark, and R. L. Huguenin (1978), Mars—Near-infrared spectral reflectance and compositional implication, *J. Geophys. Res.*, *83*(B11), 5433–5441.

McLennan, S. M. (2003), Sedimentary silica on Mars, *Geology*, *31*(4), 315–318.

McSween, H. Y., et al. (1999), Chemical, multispectral, and textural constraints on the composition and origin of rocks at the Mars Pathfinder landing site, *J. Geophys. Res.*, *104*(E4), 8679–8715.

McSween, H. Y., T. L. Grove, and M. B. Wyatt (2003), Constraints on the composition and petrogenesis of the Martian crust, *J. Geophys. Res.*, *108*(E12), 5135. doi:10.1029/2003JE002175.

Mellon, M. T., B. M. Jakosky, H. H. Kieffer, and P. R. Christensen (2000), High-resolution thermal inertia mapping from the Mars Global Surveyor Thermal Emission Spectrometer, *Icarus*, *148*(2), 437–455.

Michalski, J. R., M. D. Kraft, T. Diedrich, T. G. Sharp, and P. R. Christensen (2003), Thermal emission spectroscopy of the silica polymorphs and considerations for remote sensing of Mars, *Geophys. Res. Lett.*, *30*(19), 2008, doi:10.1029/2003GL018354.

Michalski, J. R., M. D. Kraft, T. G. Sharp, and P. R. Christensen (2005a), Palagonite-like alteration products on the Earth and Mars I: Spectroscopy (0.4–2.5 microns) of weathered basalts and silicate alteration products, *Lunar Planet. Sci.*, *XXXVI*, abstract 1188.

Michalski, J. R., M. D. Kraft, T. G. Sharp, L. B. Williams, and P. R. Christensen (2005b), Mineralogical constraints on the high-silica Martian surface component observed by TES, *Icarus*, *174*(1), 161–177.

Milliken, R. E., J. F. Mustard, and D. L. Goldsby (2003), Viscous flow features on the surface of Mars: Observations from high-resolution Mars Orbiter Camera (MOC) images, *J. Geophys. Res.*, *108*(E6), 5057, doi:10.1029/2002JE002005.

Minitti, M. E., C. M. Weitz, M. D. Lane, and J. L. Bishop (2003), Composition and spectra of several Hawaiian rock coatings, *Lunar Planet. Sci.*, *XXXIV*, abstract 1937.

Minitti, M. E., C. M. Weitz, M. D. Lane, and J. L. Bishop (2005), Rock coatings from Vulcano, a Martian analog environment, *Lunar Planet. Sci.*, *XXXVI*, abstract 1835.

Moersch, J. E., T. L. Hayward, P. D. Nicholson, S. W. Squyres, J. VanCleve, and P. R. Christensen (1997), Identification of a 10-mu m silicate absorption feature in the Acidalia region of Mars, *Icarus*, *126*(1), 183–196.

Morris, R. V., T. G. Graff, S. A. Mertzman, M. D. Lane, and P. R. Christensen (2003), Palagonitic (not andesitic) Mars: Evidence from thermal emission and VNIR spectra of palagonitic alteration rinds on basaltic rock, paper presented at Sixth International Conference on Mars, Lunar and Planet. Inst., Houston, Tex.

Morse, S. A. (1996), Kiglapait mineralogy. 3. Olivine compositions and Rayleigh fractionation models, *J. Petrol.*, *37*(5), 1037–1061.

Mustard, J. F., and J. M. Sunshine (1995), Seeing through the Dust—Martian crustal heterogeneity and links to the Snc meteorites, *Science*, *267*(5204), 1623–1626.

Mustard, J. F., S. Murchie, S. Erard, and J. Sunshine (1997), In situ compositions of Martian volcanics: Implications for the mantle, *J. Geophys. Res.*, *102*(E11), 25,605–25,615.

Mustard, J. F., C. D. Cooper, and M. K. Rifkin (2001), Evidence for recent climate change on Mars from the identification of youthful near-surface ground ice, *Nature*, *412*(6845), 411–414.

Mustard, J. F., F. Poulet, A. Gendrin, J. P. Bibring, Y. Langevin, B. Gondet, N. Mangold, G. Bellucci, and F. Altieri (2005), Olivine and pyroxene diversity in the crust of Mars, *Science*, *307*(5715), 1594–1597.

Noe Dobrea, E. Z., J. F. Bell, M. J. Wolff, and K. D. Gordon (2003), H_2O- and OH-bearing minerals in the Martian regolith: Analysis of 1997 observations from HST/NICMOS, *Icarus*, *166*(1), 1–20.

Nowicki, S. A., and P. R. Christensen (1999), Mars surface rock abundance from Thermal Emission Spectrometer (TES) mapping data, paper presented at Fifth International Conference on Mars, Lunar and Planet. Inst., Houston, Tex.

Pollack, J. B., T. Roush, F. Witteborn, J. Bregman, D. Wooden, C. Stoker, O. B. Toon, D. Rank, B. Dalton, and R. Freedman (1990), Thermal Emission-Spectra of Mars (5.4–10.5-Mu-M): Evidence for sulfates, carbonates, and hydrates, *J. Geophys. Res.*, *95*(B9), 14,595–14,627.

Poulet, F., J. P. Bibring, J. F. Mustard, A. Gendrin, N. Mangold, Y. Langevin, R. E. Arvidson, B. Gondet, C. Gomez, and Omega Team (2005), Phyllosilicates on Mars and implications for early Martian climate, *Nature*, *438*(7068), 623–627.

Presley, M. A., and P. R. Christensen (1997), Thermal conductivity measurements of particulate materials: 2. Results, *J. Geophys. Res.*, *102*(E3), 6551–6566.

Ramsey, M. S., and P. R. Christensen (1998), Mineral abundance determination: Quantitative deconvolution of thermal emission spectra, *J. Geophys. Res.*, *103*(B1), 577–596.

Rogers, D., and P. R. Christensen (2003), Age relationship of basaltic and andesitic surface compositions on Mars: Analysis of high-resolution TES observations of the Northern Hemisphere, *J. Geophys. Res.*, *108*(E4), 5030, doi:10.1029/2002JE001913.

Rogers, A. D., and P. R. Christensen (2007), Surface mineralogy of Martian low-albedo regions from MGS-TES data: Implications for upper crustal evolution and surface alteration, *J. Geophys. Res.*, doi:10.1029/2006JE002727, in press.

Rogers, A. D., P. R. Christensen, and J. L. Bandfield (2005), Compositional heterogeneity of the ancient Martian crust: Surface analysis of Ares Vallis bedrock with THEMIS and TES data, *J. Geophys. Res.*, *110*, E05010, doi:10.1029/2005JE002399.

Ruff, S. W. (1998), Quantitative thermal infrared emission spectroscopy applied to granitoid petrology, Ph.D. dissertation, Ariz. State Univ., Tempe.

Ruff, S. W. (2003), Basaltic andesite or weathered basalt: A new assessment, paper presented at Sixth International Conference on Mars, Lunar and Planet. Inst., Houston, Tex.

Ruff, S. W. (2004), Spectral evidence for zeolite in the dust on Mars, *Icarus*, *168*(1), 131–143.

Ruff, S. W., and P. R. Christensen (2002), Bright and dark regions on Mars: Particle size and mineralogical characteristics based on Thermal Emission Spectrometer data, *J. Geophys. Res.*, *107*(E12), 5127, doi:10.1029/2001JE001580.

Ruff, S. W., and V. E. Hamilton (2001), Mineralogical anomalies in Mars Nili Patera Caldera observed with Thermal Emission Spectrometer data, *Lunar Planet. Sci.*, *XXXII*, abstract 2186.

Singer, R. B. (1982), Spectral evidence for the mineralogy of high-albedo soils and dust on Mars, *J. Geophys. Res.*, *87*(B12), 159–168.

Smith, M. D., J. L. Bandfield, and P. R. Christensen (2000a), Separation of atmospheric and surface spectral features in Mars Global Surveyor Thermal Emission Spectrometer (TES) spectra, *J. Geophys. Res.*, *105*(E4), 9589–9607.

Smith, M. D., J. C. Pearl, B. J. Conrath, and P. R. Christensen (2000b), Mars Global Surveyor Thermal Emission Spectrometer (TES) observations of dust opacity during aerobraking and science phasing, *J. Geophys. Res.*, *105*(E4), 9539–9552.

Soderblom, L. A. (1992), The composition and mineralogy of the Martian surface from spectroscopic observations: 0.3 microns to 50 microns, in *Mars*, edited by H. H. Kieffer, et al., pp. 557–593, Univ. of Ariz. Press, Tucson.

Squyres, S. W., et al. (2004), The Spirit Rover's Athena science investigation at Gusev Crater, Mars, *Science*, *305*(5685), 794–799.

Tanaka, K. L., J. A. Skinner, T. M. Hare, T. Joyal, and A. Wenker (2003), Resurfacing history of the northern plains of Mars based on geologic mapping of Mars Global Surveyor data, *J. Geophys. Res.*, *108*(E4), 8043, doi:10.1029/2002JE001908.

Taylor, G. J., L. M. V. Martel, and W. V. Boynton (2006), Mapping Mars geochemically, *Lunar Planet Sci.*, *XXXVII*, abstract 1981.

Thomas, P., J. Veverka, D. Gineris, and L. Wong (1984), Dust streaks on Mars, *Icarus*, *60*(1), 161–179.

Wyatt, M. B., and H. Y. McSween (2002), Spectral evidence for weathered basalt as an alternative to andesite in the northern lowlands of Mars, *Nature*, *417*(6886), 263–266.

Wyatt, M. B., V. E. Hamilton, H. Y. McSween, P. R. Christensen, and L. A. Taylor (2001), Analysis of terrestrial and Martian volcanic compositions using thermal emission spectroscopy: 1. Determination of mineralogy, chemistry, and classification strategies, *J. Geophys. Res.*, *106*(E7), 14,711–14,732.

Wyatt, M. B., H. Y. McSween, J. E. Moersch, and P. R. Christensen (2003), Analysis of surface compositions in the Oxia Palus region on Mars from Mars Global Surveyor Thermal Emission Spectrometer Observations, *J. Geophys. Res.*, *108*(E9), 5107, doi:10.1029/2002JE001986.

Wyatt, M. B., H. Y. McSween, K. L. Tanaka, and J. W. Head (2004), Global geologic context for rock types and surface alteration on Mars, *Geology*, *32*(8), 645–648.

J. L. Bandfield and P. R. Christensen, Department of Geological Sciences, Arizona State University, Campus Box 6305, Tempe, AZ 85287-6305, USA.

A. D. Rogers, Division of Geological and Planetary Sciences, California Institute of Technology, MC 150-21, Pasadena, CA 91125, USA. (drogers@gps.caltech.edu)